NASA TECHNICAL MEMORANDUM

NASA TM X-62,294

NASA TM X-62,294

LASER DOPPLER VELOCIMETER INVESTIGATION OF TRAILING VORTICES BEHIND A SEMI-SPAN SWEPT WING IN A LANDING CONFIGURATION

D. L. Ciffone, K. L. Orloff and G. R. Grant

Ames Research Center
Moffett Field, Calif. 94035

August 1973

LASER DOPPLER VELOCIMETER INVESTIGATION OF TRAILING VORTICES BEHIND A SEMI-SPAN SWEPT WING IN A LANDING CONFIGURATION

By
D. L. Ciffone, K. L. Orloff and G. R. Grant

Abstract

Measured axial and tangential velocity profiles in the near wake vortices of a semi-span model of the Convair 990 wing in the NASA-Ames 7- by 10-foot wind tunnel are presented. A scanning laser Doppler velocimeter was used to obtain data at two different downstream stations (0.49 and 1.25 wing spans) at various angles of attack and configurations from wing alone to wing plus nacelles, anti-shock bodies, and flaps deflected 27 degrees (landing configuration). It is shown that the velocity distributions within the wake are quite sensitive to span loading. Specifically, it is illustrated that an aircraft flying at a given lift coefficient (C_L), can substantially reduce its trailing vortex upset potential by deploying its flaps and altering its flight attitude to maintain the same C_L. This might be taken into consideration along with performance and noise considerations in the selection of aircraft approach L/D's.

NOMENCLATURE

b	Wing span
c	Wing reference chord
C_L	Lift coefficient
f_{D_θ}	Doppler frequency - vertical component
f_{D_x}	Doppler frequency - horizontal component
L/D	Lift-to-drag ratio
S	Wing surface area
U_∞	Wind tunnel mainstream velocity
V_x	Axial velocity component
V_θ	Tangential velocity component
W	Basic CV-990 wing
WF = 27	Wing plus flaps at 27 degrees
WNS	Wing plus nacelles plus anti-shock bodies
WNF = 27	Wing plus nacelles plus flaps at 27 degrees
WNSF = 27	Wing plus nacelles plus anti-shock bodies plus flaps at 27 degrees
WINF = 27	Wing plus inboard nacelle plus flaps at 27 degrees
X	Streamwise ordinate, aft from trailing edge
Y	Spanwise ordinate, inboard from wing tip
Z	Normal to mainstream, positive below lower surface, origin at wing tip T.E.
Å	Angstrom units of wavelength
α	Angle of attack (referenced to the top of the fuselage)
θ	Intersection angle of the laser cross beams

Introduction

A considerable amount of information documenting the structure of wake turbulence has been produced over the last several years. Quantitative detailing of the flow has, however, been primarily restricted to generating airfoils with simple near-rectangular or elliptic span loadings. The need for experimental velocity distributions from models of wings representative of today's modern transport aircraft is the rationale for this memorandum.

A dual-beam backscatter laser Doppler velocimeter (LDV) has been used to scan and measure the velocity distributions in the near wake of a Convair-990 semi-span model (Fig. 1) in the NASA-Ames 7- by 10-foot wind tunnel. This LDV instrument has previously been used to measure the velocity distribution in the wake of a rectangular airfoil[1,2]. The effects of shock bodies, nacelles, flap deflection, and angle of attack at downstream distances of X/b = 0.49 and 1.25 were investigated. Reynolds number per foot was nominally 378,000. Comparison of the present test results with previous three-wire anemometer measurements[3] in the wake of the same swept wing model are presented. The complication of vortex movement within the test section has been overcome as a result of the spatial scanning capability of the laser velocimeter.

A conclusion previously deduced from LDV testing[2] is that profile drag will manifest itself as: a) an increased defect in the axial velocity distribution; and b) a reduction in $V_{\theta max}/U_{\infty}$ resulting from the incorporation of turbulence (generated at the wing) into the vortex structure. The latter effect is evident when the turbulence is introduced into a region

of high vorticity concentration in the span loading. The results of the present tests will be discussed with due consideration to these observations, as well as to the effect of span loading on the vortex structure.

Experimental Apparatus and Procedure

A semi-span model of the Convair-990 wing was mounted vertically from the floor of the NASA-Ames 7- by 10-foot wind tunnel, as illustrated in Fig. 1. Details of the wing model are given in Fig. 2 and Table I. The laser system was restricted to the location of the optical window; hence, the wing model was placed in a forward position in the test section to allow data to be obtained at the maximum aft X/b (X/b = 1.25). Data were also obtained at an X/b = 0.49, with the model mounted close to the center of the test section. At each location both the LDV measuring station and model position were well within the test section to insure flow uniformity.

LDV scanning was performed in a direction normal to the tunnel centerline, with the upper wing surface closest to the window through which the measurements were taken. The Doppler information was processed on two separate spectrum analyzers as the focal point of the velocimeter was continuously traversing the vortex. The scan automatically reversed at end limits which were preset to contain the flow area of interest. The spectrum analyzer traces (one each for the axial and tangential velocities) and the voltage representing the position of the test point were continuously recorded on magnetic tape.

Particulate scattering material was introduced into the diffuser section of the wind tunnel by means of a mineral oil smoke generator, and

recirculation of the air provided for a light concentration of the oil vapor throughout the tunnel. The strong centrifugal action of the vortex distinguished the core as a small region lacking scattering material. As a result, the laser beams were not illuminated at the very center of the vortex, but it was possible to visually observe when a traverse was made directly through the center of the vortex, and the event was marked on a separate recording channel of the magnetic tape. These "core penetration" events could then be transferred onto an oscillograph record from which the data were reduced (see Ref. 2 for details).

Tufts were placed from the 1/4-chord position to the trailing edge of the wing, from the tip inboard about 20% of the semi-span. It was observed that this portion of the wing was at least partially stalled for all configurations at angles of attack of 4.3 degrees or greater. For angles between 4.3 and 3.3 degrees, the stall was intermittent, while at angles of 3.3 and less, the wing was generally unstalled. All angles of attack are referenced to the top of the fuselage which was parallel to the longitudinal axis of the model. The wing root and tip chords were at 4 and 2 degrees incidence, respectively, relative to the fuselage reference line. In all circumstances, tip-stall and associated flow separation could immediately be detected on the spectrum analyzer traces by significant broadening and distortion of the Doppler signal. A consistent correspondence existed between visual observations of this flow separation and the broadening of the Doppler signal. The uncertainty which could arise in interpreting vortex velocity profiles from the Doppler signals of this unsteady flow precluded any LDV measurements for angles of attack greater than 4.3 degrees.

Data Reduction and Presentation

The measured Doppler frequency is linearly related to the velocity component perpendicular to the bisector of the angle formed by the crossed beams and lies within the plane formed by these beams. The necessary equations are

$$V_x = \frac{(5145\ \text{Å})}{2} \frac{f_{D_x}}{\sin \theta/2} \; ; \quad V_\theta = \frac{(4880\ \text{Å})}{2} \frac{f_{D_\theta}}{\sin \theta/2}$$

where x and θ refer to axial and tangential values, respectively. These expressions will accurately represent the flow field when an "on-diameter" penetration of the vortex is made. The angular dependence, sin θ/2, is a function of the distance of the crosspoint from the transmitting lens.

Signal processing was accomplished with two identical spectrum analyzer systems. The vertical (frequency content) and horizontal (sweep position) outputs of each analyzer were recorded on an oscillograph. Voltage from the linear potentiometer (driven by the scanning lens carriage) was also recorded. This voltage (representing the tunnel location of the test point) and the frequency information from the spectrum analyzer were reduced to yield velocity and spatial position relative to the wing trailing edge.

All velocity distributions are presented as fractions of free stream velocity, U_∞, and location, Z, relative to the trailing edge (Z = 0), normalized to the span, b. A positive value for Z/b then indicates a location on the side of the lower surface of the wing, whereas a negative value is associated with positions on the side of the upper wing surface. The bulk of the data are presented in the Appendix with the exception of Figs. 3a and 3b which are representative of the data and are discussed in detail below. Table II serves as an index to this data and lists pertinent

test parameters. The average of the maximum tangential velocity normalized by freestream velocity and lift coefficient

$$\frac{1}{2C_L}\left[\left(\frac{V_\theta}{U_\infty}\right)_{\max \text{ above wing}} + \left(\frac{V_\theta}{U_\infty}\right)_{\max \text{ below wing}}\right] = \frac{V_{\theta max}}{U_\infty C_L}$$

is presented, as well as the difference,

$$\left(\frac{V_x}{U_\infty}\right)_{\text{core}} - 1,$$

between axial core velocity and free stream velocity.

Results and Discussion

Typical velocity profiles are presented in Figs. 3a and 3b for both the flaps-retracted and flaps-deployed configurations. It can be seen that the repeatability of the data from run to run is excellent, and the vortex structure is well defined. The data show a higher total angular momentum and axial velocity defect for the flaps-deployed configuration, but no perceptible change in maximum tangential velocity. While deployment of flaps increases circulation (and should increase $\left[\frac{V_\theta}{U_\infty}\right]_{max}$), it also alters the lift distribution, moving the center of vorticity inboard along the span resulting in a less concentrated vortex (which should decrease $\left[\frac{V_\theta}{U_\infty}\right]_{max}$). The net effect at the particular station and test conditions shown on the figures appears as no significant change in $\left[\frac{V_\theta}{U_\infty}\right]_{max}$. The three percent increase in axial velocity defect is due to the slight increase in profile drag associated with the 27-degree flap deployment. It is conjectured that the tendency of the tangential velocity to increase in the potential flow region below the wing is due to a compression of the vortex streamlines as the vortex sinks through the relatively stationary flow.

Also shown in Figs. 3a and 3b for comparative purposes are the hot-wire data of Ref. 3 obtained in the same facility and with the same model. It is believed that the combination of vortex movement and the subsequent time-averaging of the hot-wire data are responsible for the apparent loss of detail near the vortex core and the suppression of measured velocities.

The remainder of the test data is presented in the Appendix.

The measured variation of $\frac{V_{\theta max}}{U_\infty}$ with angle of attack, α, is plotted in Fig. 4a for the complete configuration with flaps deployed (WNSF = 27). The corresponding lift coefficient is also shown (as presented in Ref. 4). If one assumes a linear variation of $\frac{V_{\theta max}}{U_\infty}$ with angle of attack (as indicated in the findings of Refs. 2 and 3) and the data is faired, as shown in Fig. 4a, then Fig. 4b indicates that for a given span loading, the nondimensional value $\frac{V_{\theta max}}{C_L U_\infty}$ appears constant with varying α. Interestingly enough, this constant value of 0.81 agrees quite closely to that measured for a rectangular planform wing (Ref. 2). This apparent removal of the dependence upon C_L, although not of paramount importance, is useful and is employed in subsequent figures when appropriate.

Figure 5 shows the variation of core axial velocity with angle of attack for the same configuration (WNSF = 27). It is seen that in the near wake (for the low angles of attack investigated) the axial velocity defect increases with increasing angle of attack. Data above $\alpha = 4.3°$ were not recorded since there was evidence of model tip stall at these higher angles. It has been shown (Ref. 5) that in the near wake the incremental axial velocity can be either forward (defect) or rearward (enhancement), depending on the relative contributions of induced and

profile drag coefficients. For the angle of attack range investigated in this test, a momentum defect in the vortex core was observed, and this defect increased with increasing angle of attack. Although profile drag increase with angle of attack is negligible relative to induced drag increase, momentum defects associated with it are directly introduced into the vortex core, whereas the momentum defect associated with the induced drag is distributed across the trailing wake with only a small percentage of it present in the core. Considering the incidence angles of the wing chord plane and frontal areas of the nacelles, pylons, anti-shock bodies and flaps, it might be expected that the angle of attack associated with minimum profile drag for this configuration will be at about -2°, and the defect data do indicate that such a minimum may exist in this region. The data point for the aft station indicates that the velocity defect is not increasing (and probably decreasing) with downstream distance for this configuration.

The effect of downstream distance on maximum tangential and axial core velocity as the model is built up from the wing alone to the complete configuration with flaps extended is shown in Fig. 6. Here the non-dimensional tangential velocity, $\frac{V_\theta}{U_\infty}$, has been normalized by lift coefficient, C_L, to allow a given configuration to be compared at different angles of attack for two downstream locations. Also shown in this figure is a dashed line which represents a $\frac{V_{\theta max}}{C_L U_\infty} \sim (\frac{X}{b})^{1/2}$ relationship which can be shown to be the rotational velocity dependence at the core radius of a forced laminar viscous trailing vortex (Ref. 6). In general, the slope of the data tend to verify this dependence. The configuration appears to have little influence on the dependence of $\frac{V_{\theta max}}{C_L U_\infty}$ upon $\frac{X}{b}$ with the exception of the clean wing data.

The variation of axial velocity with downstream location is less systematic. The flaps-retracted data, W and WNS, show an increasing defect with downstream distance, while the data for the flaps extended indicate a defect reduction with $\frac{X}{b}$. The data for each configuration are for constant angle of attack; the data for WF = 27 and WNF = 27 at $\frac{X}{b} = 0.49$ have been corrected to $\alpha = 3.3°$ and $4.3°$, respectively, by use of Fig. 5. It is suggested by Fig. 6 that nacelles have only a small influence upon the streamwise change in the axial velocity profile; the effect of the anti-shock bodies is greater at the aft station, while the effect of flaps is greater at the forward station. Apparently, the streamwise evolution of the axial profile is quite sensitive to the initial conditions in the very near wake.

The effect of downstream distance on the near wake velocity distributions is shown in Figs. 7 and 8. The data for the wing along (Fig. 7, W) shown an intense vortex with subsequent rapid decay as one proceeds downstream. The full configuration with flaps retracted (Fig. 8, WNS) exhibits a lower initial intensity near the core, and a slower streamwise decay. The trends are probably the result of additional boundary layer turbulence (from nacelles and anti-shock bodies) being introduced into the vortex.

A relatively large amount of profile drag (and the associated turbulence injection) is indicated by the axial velocity defect for the complete configuration. The reason for the appearance of the axial defect at a position other than the vortex center for the WNS configuration (at $\frac{X}{b} = 0.49$) is not understood. It might be a result of incomplete roll-up of the vortex sheet.

Figure 9 illustrates the effects of flap deflection and anti-shock bodies on vortex velocity profiles. Here again, it is apparent that for the test conditions shown on the Figure, the effect of flap deployment on tangential velocity is not discernible. This is due to the counteracting effects of span load change (less concentrated vortex) and lift coefficient increase (greater circulation). Although the flap deflection does contribute an induced drag increment to the wake momentum defect, only a small portion of this defect is realized in the near field vortex.

At the low freestream velocity of these tests, the shock bodies are very inefficient aerodynamically, and their profile drag contribution is evident in the amount of axial velocity defect which is present. In tests performed on a rectangular planform wing (Ref. 2) this increased defect due to the profile drag of a dissipator panel was closely associated with a reduction in $\frac{V_{\theta max}}{U_\infty}$, especially at downstream distances greater than one span. In tests on the present model, no such effects upon the tangential velocity distribution were observed. This is, however, not surprising when one considers that the defect generated by the shock bodies is nearly six times smaller than that resulting from the dissipator panel. Furthermore, the dissipator panel was installed at the wing tip of the rectangular wing which is the location of extremely high vorticity concentration. The test model, however, has the shock bodies located in regions removed from the center of vorticity.

It has been possible with the present model to configure it in such a manner as to make it representative in planform to various

different modern-day aircraft. While it is realized that there are discrepancies in the actual wing and flap details, as well as the nacelle-pylon relative size and placement, and that account has not been made for either leading edge devices in the landing configuration or powered nacelle effects, the opportunity to make configuration comparisons was explored, in the hope that it would indicate obvious differences in the vortex velocity profiles for different type commercial aircraft currently in use. The results are presented in Fig. 10. Listed on the figure are the configuration tested and the type of aircraft that relates to it. The tangential velocities have been normalized by lift coefficient to allow a comparison of data obtained at different angles of attack. It is surprising that the "clean" wing configuration (WF = 27) yields the vortex with the least concentration of vorticity. It is conjectured that the presence of nacelles (and shock bodies) at the low angles of attack tested reduced the model spanwise flow, and consequently may have increased the wing efficiency. Both the total angular momentum and maximum tangential velocity are greater for the configurations with nacelles. There are no large differences in the tangential profiles of the nacelled configurations normalized to the model geometry and test conditions. Direct comparisons of tangential profiles for the various types of aircraft listed in the figure can be made to a first order of approximation by ratioing the test U_∞, C_L, and b by those appropriate to the aircraft of interest.

The axial velocity profiles verify once again that the profile drag associated with the anti-shock bodies results in the largest core velocity defect. This was also shown in Fig. 9. The profile drag of the nacelles

does cause an additional velocity defect, but it is not of the same magnitude as that from the anti-shock bodies.

Previous figures have shown the effect of flap deflection on velocity profile for a given angle of attack. To decouple the effects of span load change and lift coefficient change, both associated with flap deployment, Fig. 11 presents the effects of span loading (flap deflection) at a constant lift coefficient. While both configurations represent a constant value for circulation, the effect of unloading the outer portion of the wing with flap deflection is to reduce the maximum tangential velocity considerably and to spread the vorticity. Figure 12 presents span loadings representative of those associated with the velocity profiles of Fig. 11. These span loadings are theoretical approximations of the lift distribution as computed by the vortex-lattice technique outlined in Ref. 7. The inboard movement of the span loading and consequent unloading of the outer portion of the wing with flap deflection is evident. The significance of the results illustrated in Fig. 11 is to point out that a given airplane flying at a given C_L can substantially reduce its trailing vortex upset potential by deploying its flaps and altering its flight attitude while maintaining its C_L. Presumably, the use of more and more inboard flaps would reduce the vortex hazard even more. These ideas and findings might be taken into consideration along with performance and noise considerations in the selection of aircraft approach L/D's.

The axial velocity profiles indicate a slightly smaller defect with flaps deflected which is largely an angle of attack effect as illustrated in Fig. 6.

Summary

A scanning laser Doppler velocimeter has been used to measure the axial and tangential velocity profiles at two different streamwise locations in the near wake of a Convair-990 wing. The effects of configuration build-up, span loading, angle of attack and downstream position have been investigated. The following results were obtained for the model and conditions tested:

a) Flap deflection of 27 degrees had no noticeable effect on vortex maximum tangential velocity, $V_{\theta max}$, (although a higher total angular momentum was evident) due to the cancelling effect of increased lift coefficient and modified span loading; an increase in core axial velocity defect of ~.03 U_∞ was evident.

b) The addition of anti-shock bodies did not effect $V_{\theta max}$, but did increase the axial defect by ~.10 U_∞.

c) The presence of nacelles increased $V_{\theta max}$, total angular momentum, and axial velocity defect slightly.

It is shown that the effect of span loading on vortex characteristics is pronounced. A given aircraft flying at the same lift coefficient at two different flight attitudes can significantly change the upset potential of its trailing vortex.

Future tests are planned to further explore the effect of span loading on the near, as well as the far, wake properties.

REFERENCES

1. G. R. Grant and K. L. Orloff: "A Two-Color, Dual Beam Backscatter Laser Doppler Velocimeter"; NASA TM X-62,254; March 1973.

2. K. L. Orloff and G. R. Grant: "The Application of Laser Doppler Velocimetry to Trailing Vortex Definition and Alleviation"; NASA TM X-62,243; February 1973.

3. N. A. Chigier and V. R. Corsiglia: "Wind-Tunnel Studies of Wing Wake Turbulence"; Jour. Aircraft, 9, 820 (1972).

4. N. A. Chigier and V. R. Corsiglia: "Wind-Tunnel Test Data for Wing Trailing Vortex Flow Survey"; NASA TM X-62,148; May 1972.

5. C. E. Brown: "Aerodynamics of Wake Vortices"; AIAA J., 11, 531 (1973).

6. B. G. Newman: "Flow in a Viscous Trailing Vortex"; Aero. Quart., 10, 149 (1959).

7. G. R. Hough: "Remarks on Vortex-Lattice Methods"; Jour. Aircraft, 10, 314 (1973).

TABLE I

Model Geometry

CV-990 wing	
Semi-span	91.5 cm (36 in.)
Reference chord, c = S/b	31.5 cm (12.4 in.)
Aspect ratio	6.2
Taper ratio	0.26
Incidence, root	4°
tip	2°
Section, root	NACA 0011-64
tip	NACA 0008-64
Trailing edge flap	type, plain deflection 27°

TABLE II

Figure Index for Data Curves

Figure	Configuration	X/b	α (deg.)	C_L	$\frac{V_{\theta max}}{U_\infty C_L}$	$(\frac{V_x}{U_\infty})_{core} - 1$	U_∞ m/sec
3a	WNS	1.25	4.3	.20	.96	-.100	18.25
3b	WNSF = 27°	1.25	4.3	.39	.49	-.130	18.37
A1	WNF = 27°	1.25	4.3	.39	.43	-.070	17.98
A2	WINF = 27°	1.25	3.3	.37	.52	-.085	19.36
A3	WF = 27°	1.25	3.3	.37	.39	-.055	18.20
A4	W	1.25	3.3	.15	1.00	-.070	18.22
A5	W	.49	3.3	.15	1.75	-.040	21.19
A6	WF = 27°	.49	1.3	.30	.72	-.050	21.92
A7	WNF = 27°	.49	1.3	.30	.90	-.050	22.81
A8	WNSF = 27°	.49	1.3	.30	.78	-.060	22.15
A9	WNSF = 27°	.49	-1.0	.20	.64	-.030	20.10
A10	WNSF = 27°	.49	1.0	.27	1.04	-.060	20.41
A11	WNSF = 27°	.49	3.0	.358	.74	-.110	20.28
A12	WNSF = 27°	.49	2.0	.315	.937	-.080	19.68
A13	WNS	.49	4.3	.235	1.175	-.050	23.80

Figures A1 through A13 appear in the Appendix

Nominal free stream velocity, U_∞, 20.18 m/sec (66.21 fps)

Nominal Reynolds no./foot, 378,000 $ft.^{-1}$

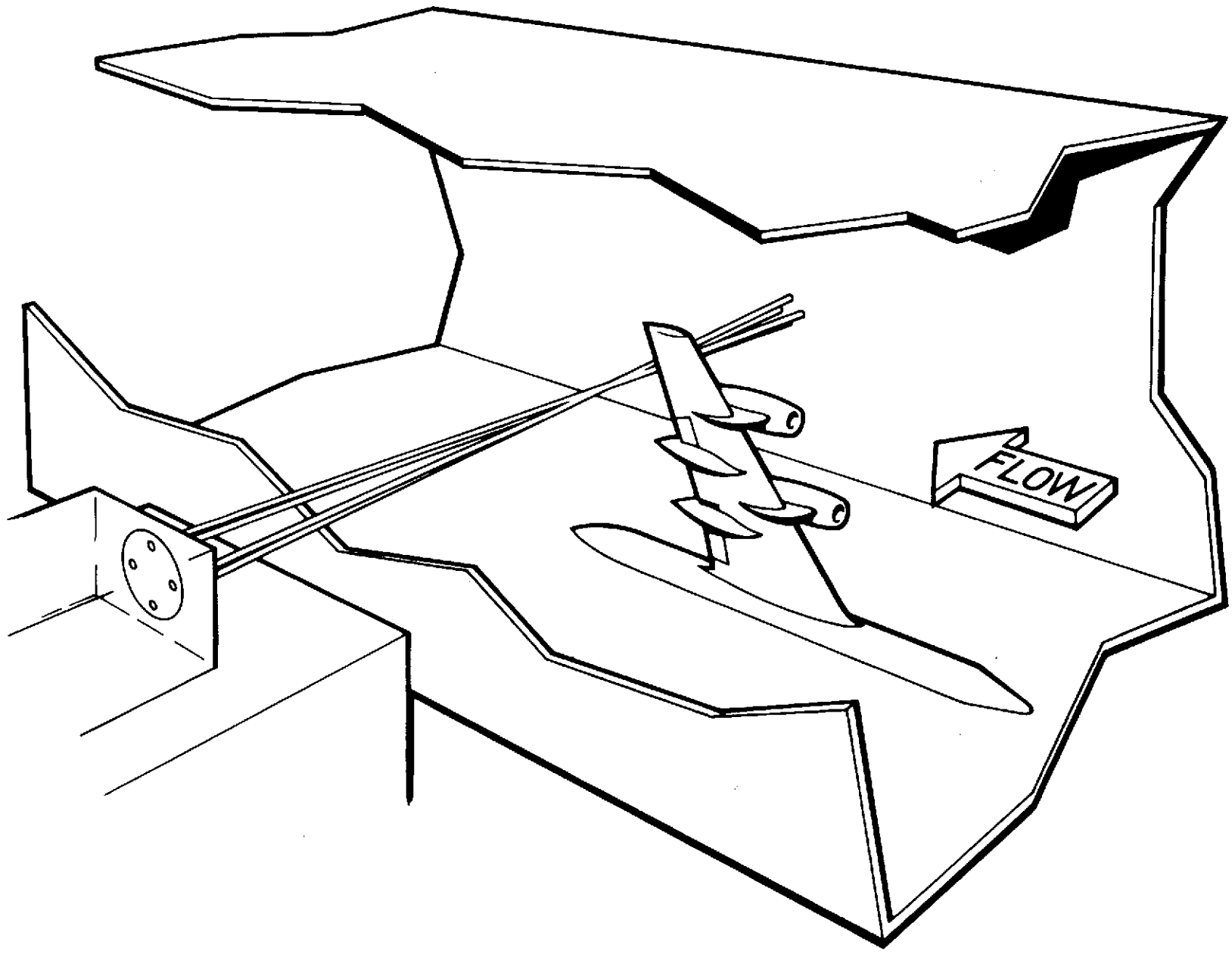

Figure 1 - Installation schematic showing semi-span model in Ames 7- by 10-foot wind tunnel and location of scanning LDV.

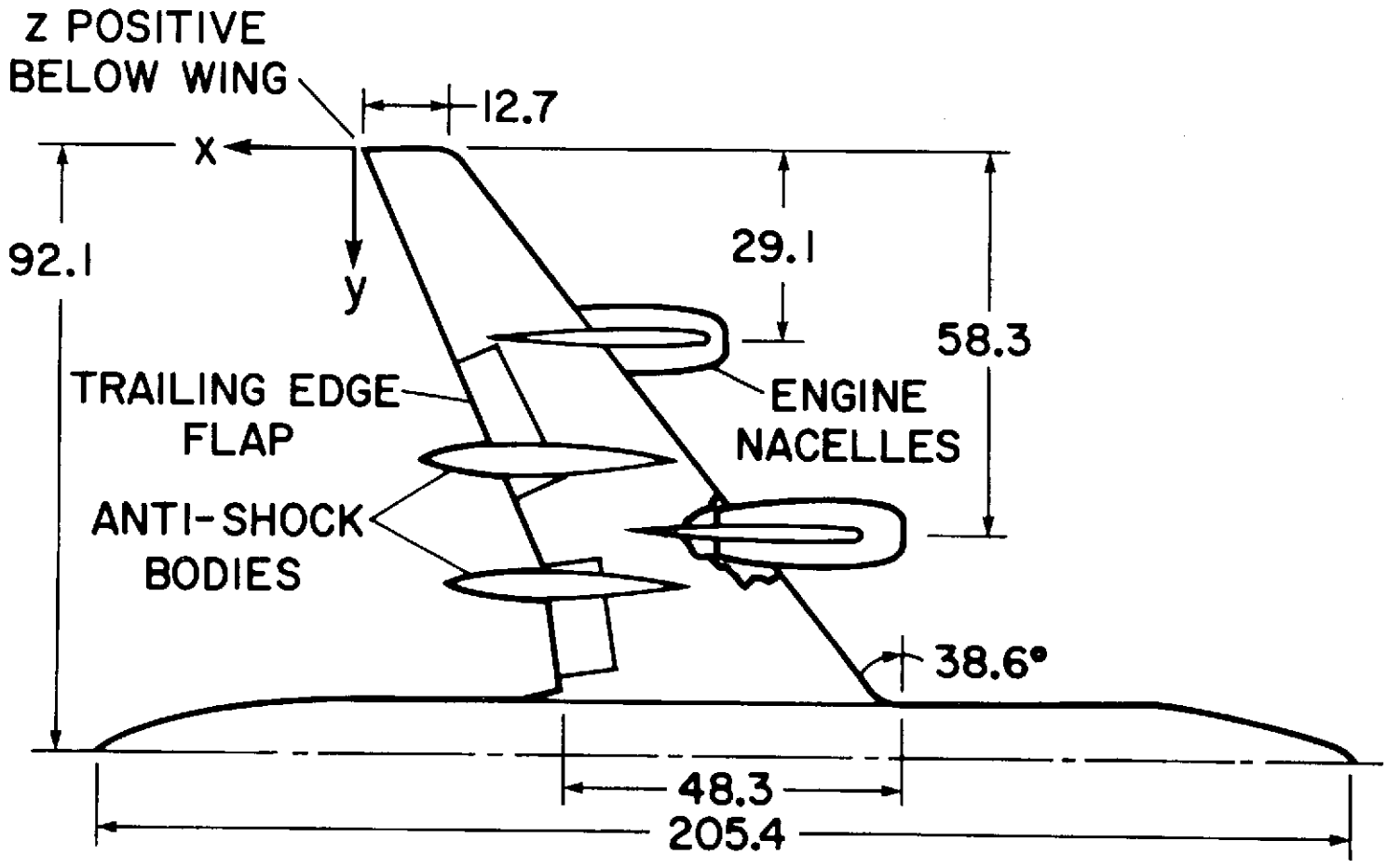

Figure 2 - Semi-span model of CV-990 aircraft showing location of engine nacelles, antishock bodies and flaps.

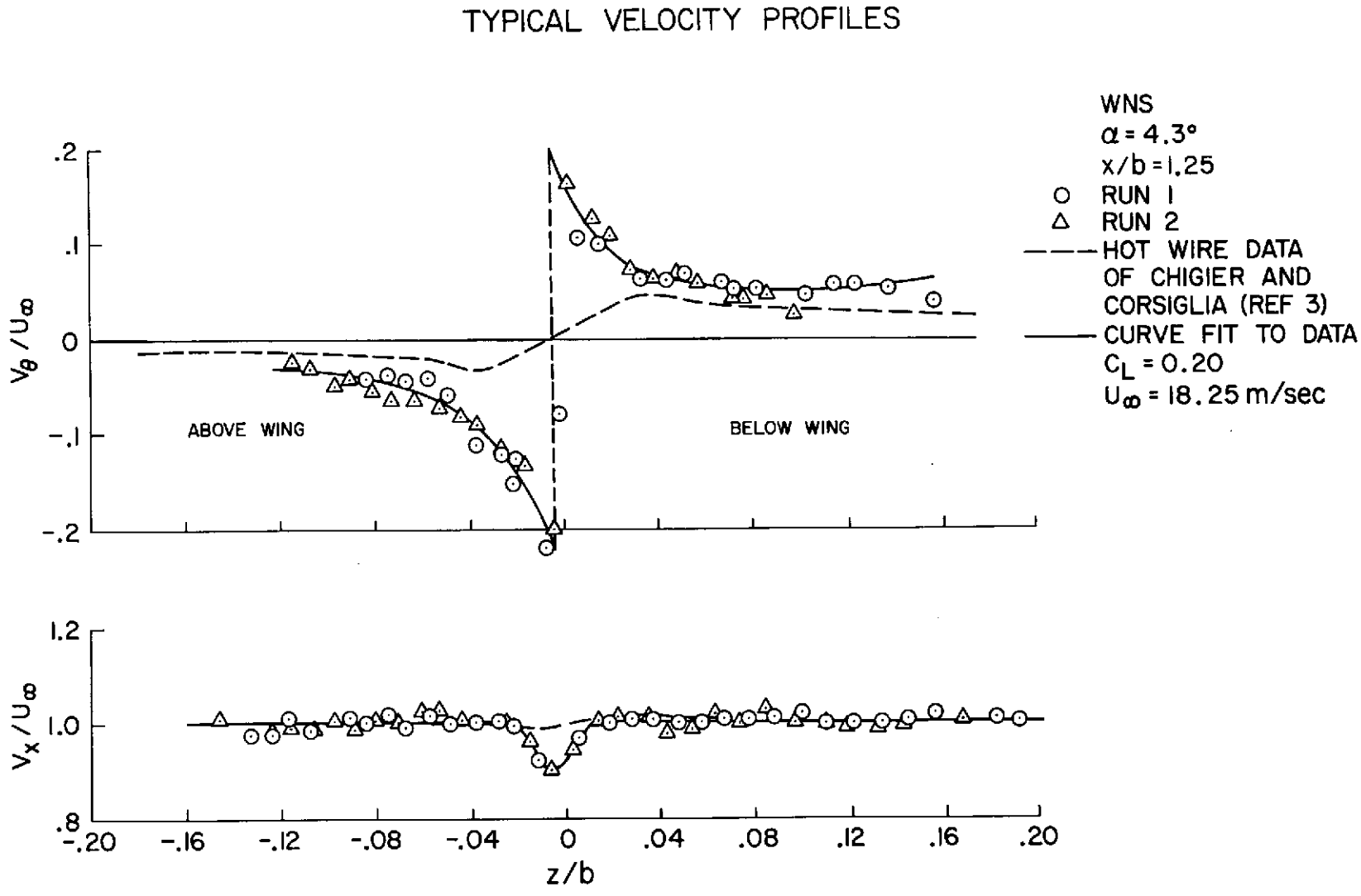
TYPICAL VELOCITY PROFILES
WNS
α = 4.3°
x/b = 1.25
RUN 1
RUN 2
HOT WIRE DATA OF CHIGIER AND CORSIGLIA (REF 3)
CURVE FIT TO DATA
C_L = 0.20
U_∞ = 18.25 m/sec
ABOVE WING
BELOW WING
V_θ / U_∞
V_x / U_∞
z/b
.2
.1
0
-.1
-.2
1.2
1.0
.8
-.20
-.16
-.12
-.08
-.04
0
.04
.08
.12
.16
.20

Figure 3a

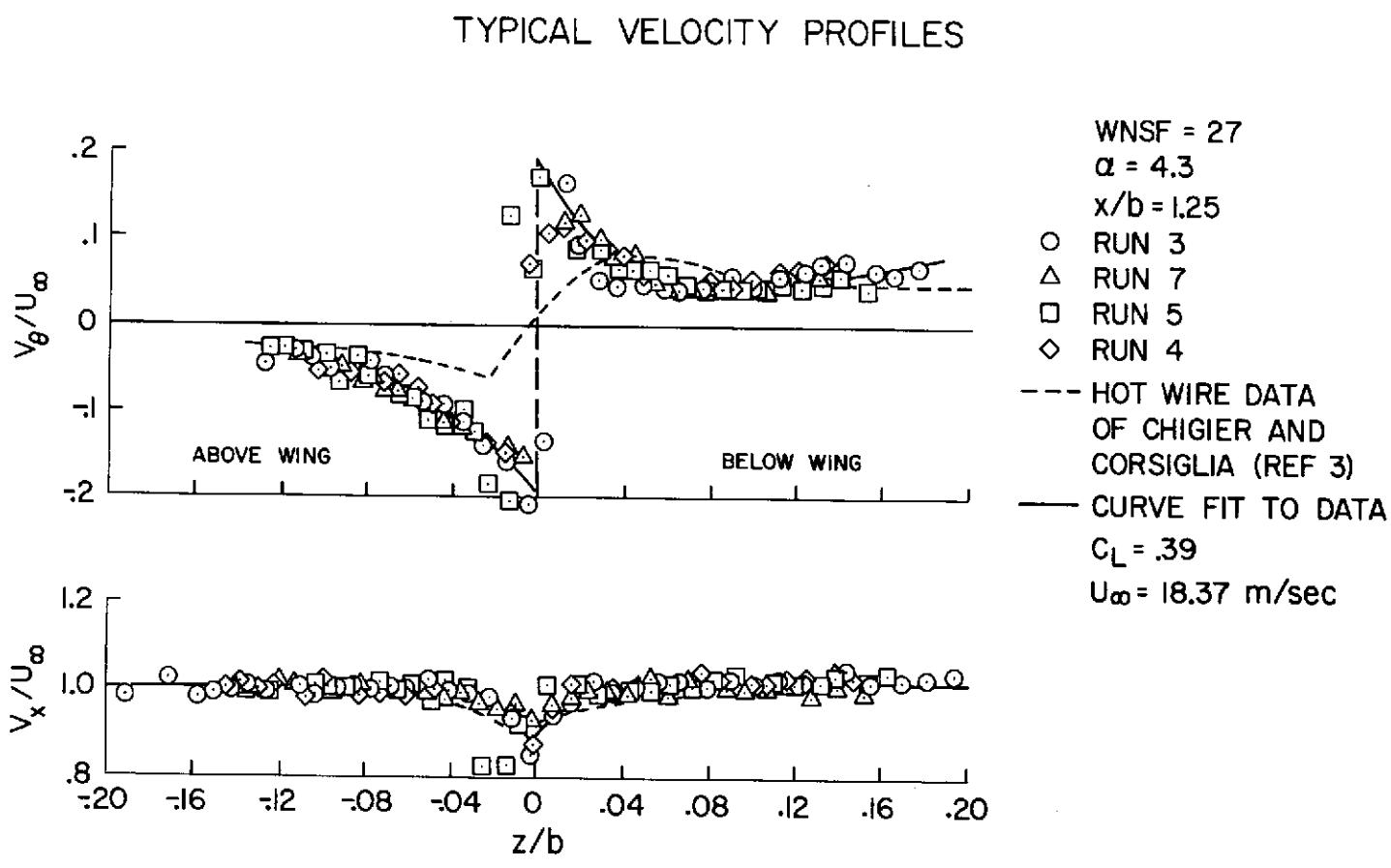
TYPICAL VELOCITY PROFILES
.2
.1
0
-.1
-.2
V_θ/U_∞
ABOVE WING
BELOW WING
1.2
1.0
.8
V_x/U_∞
-.20
-.16
-.12
-.08
-.04
0
.04
.08
.12
.16
.20
z/b
WNSF = 27
α = 4.3
x/b = 1.25
RUN 3
RUN 7
RUN 5
RUN 4
HOT WIRE DATA OF CHIGIER AND CORSIGLIA (REF 3)
CURVE FIT TO DATA
C_L = .39
U_∞ = 18.37 m/sec

Figure 3b

EFFECT OF ANGLE OF ATTACK ON MAXIMUM TANGENTIAL VELOCITY

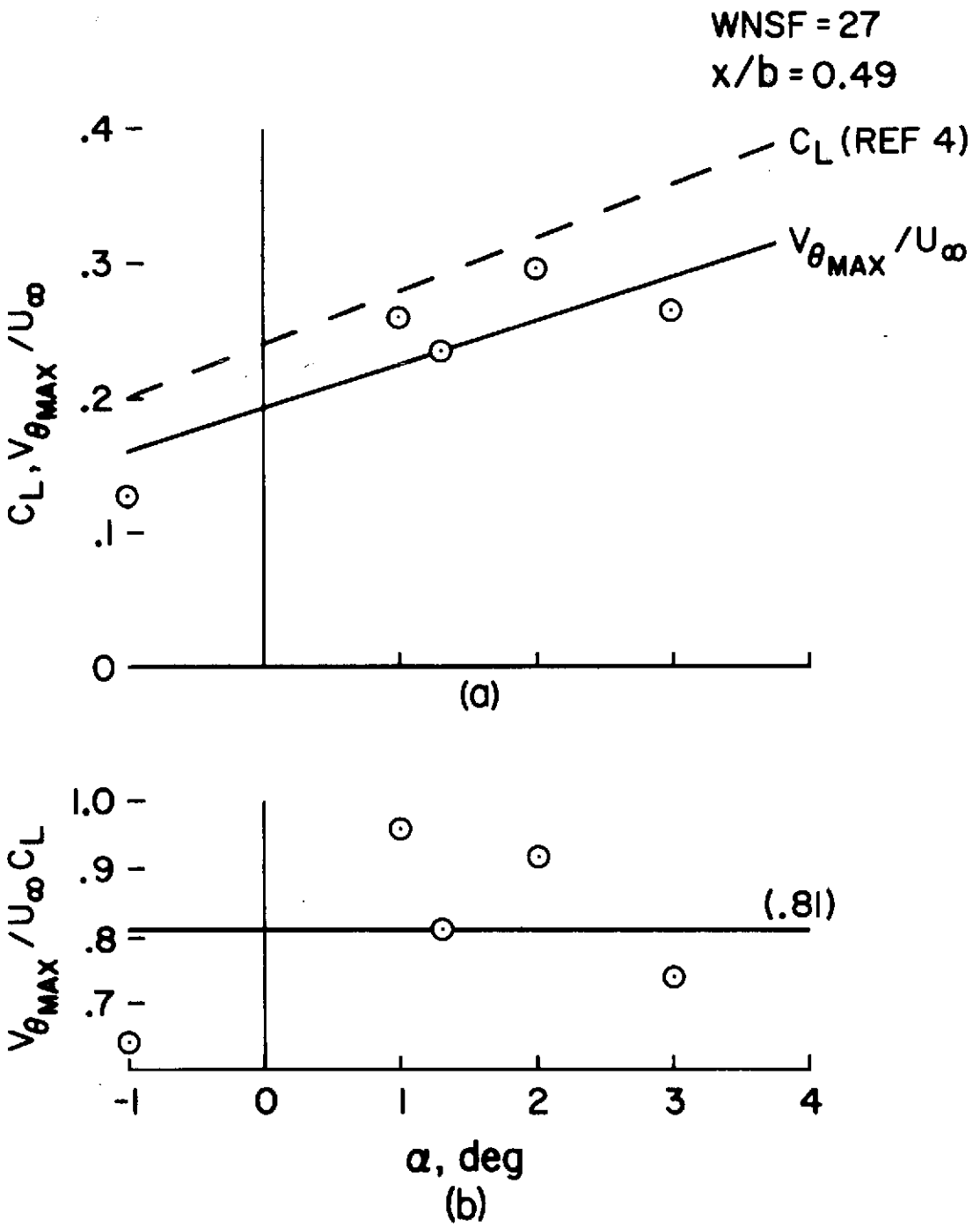

Figure 4

EFFECT OF ANGLE OF ATTACK ON CORE AXIAL VELOCITY

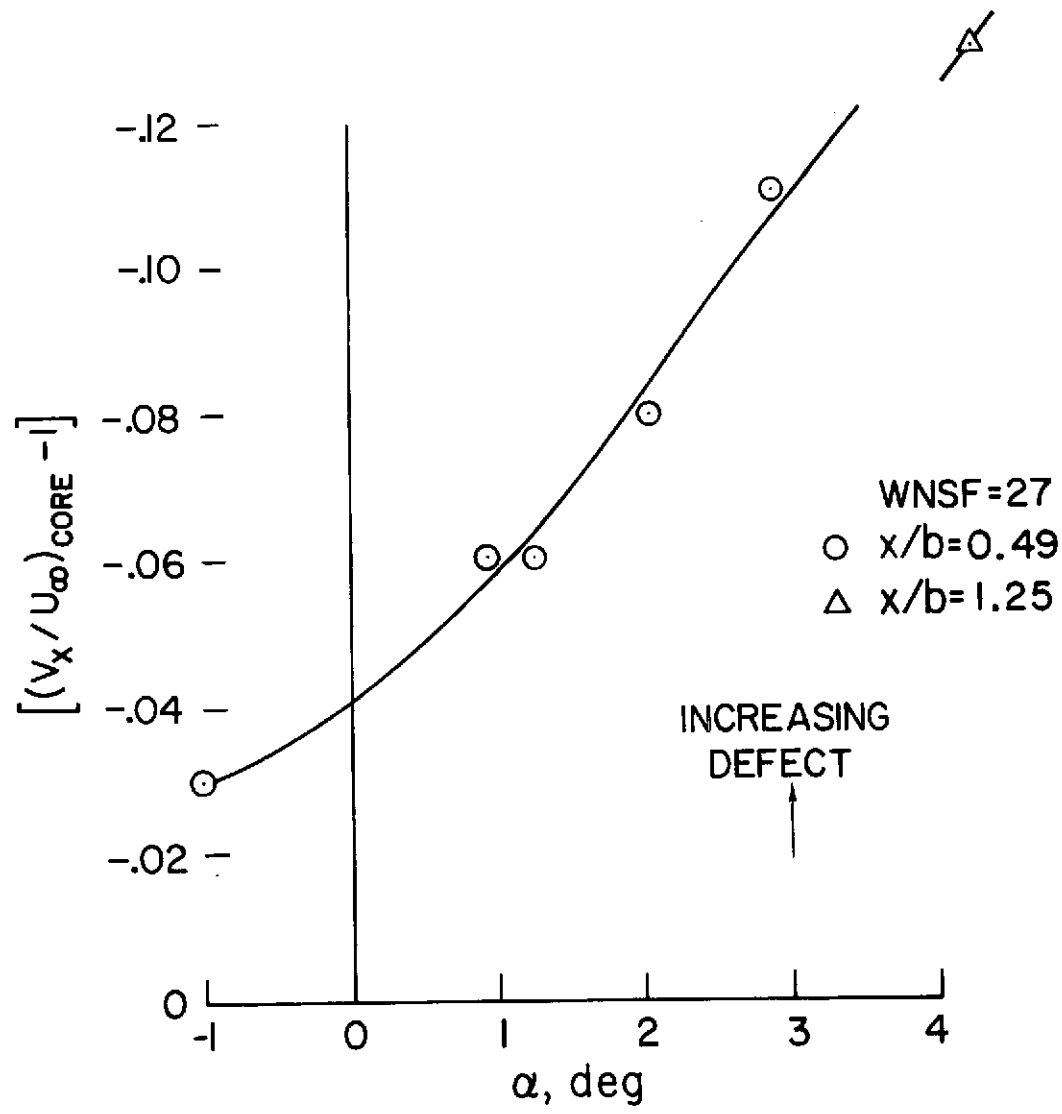

Figure 5

EFFECT OF DOWNSTREAM DISTANCE ON MAXIMUM TANGENTIAL AND AXIAL CORE VELOCITIES WITH MODEL BUILD-UP

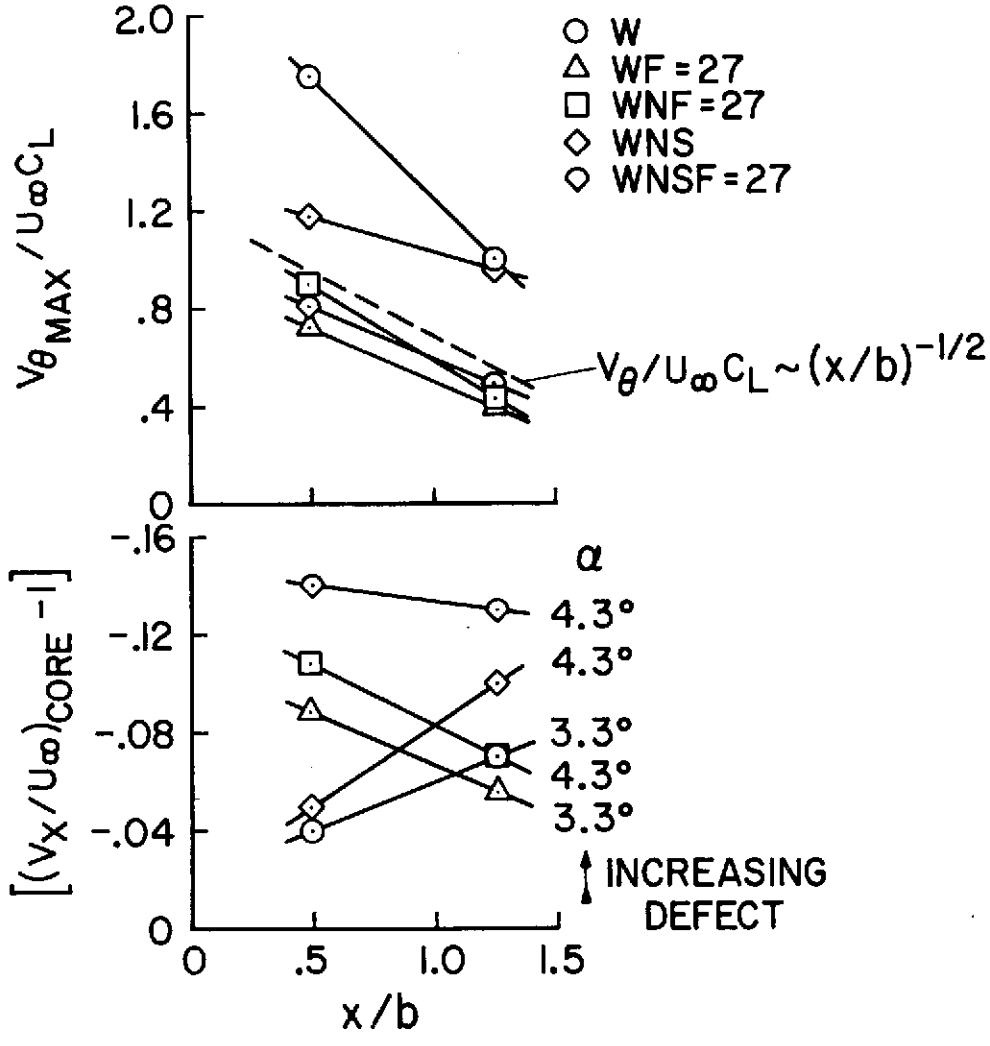

Figure 6

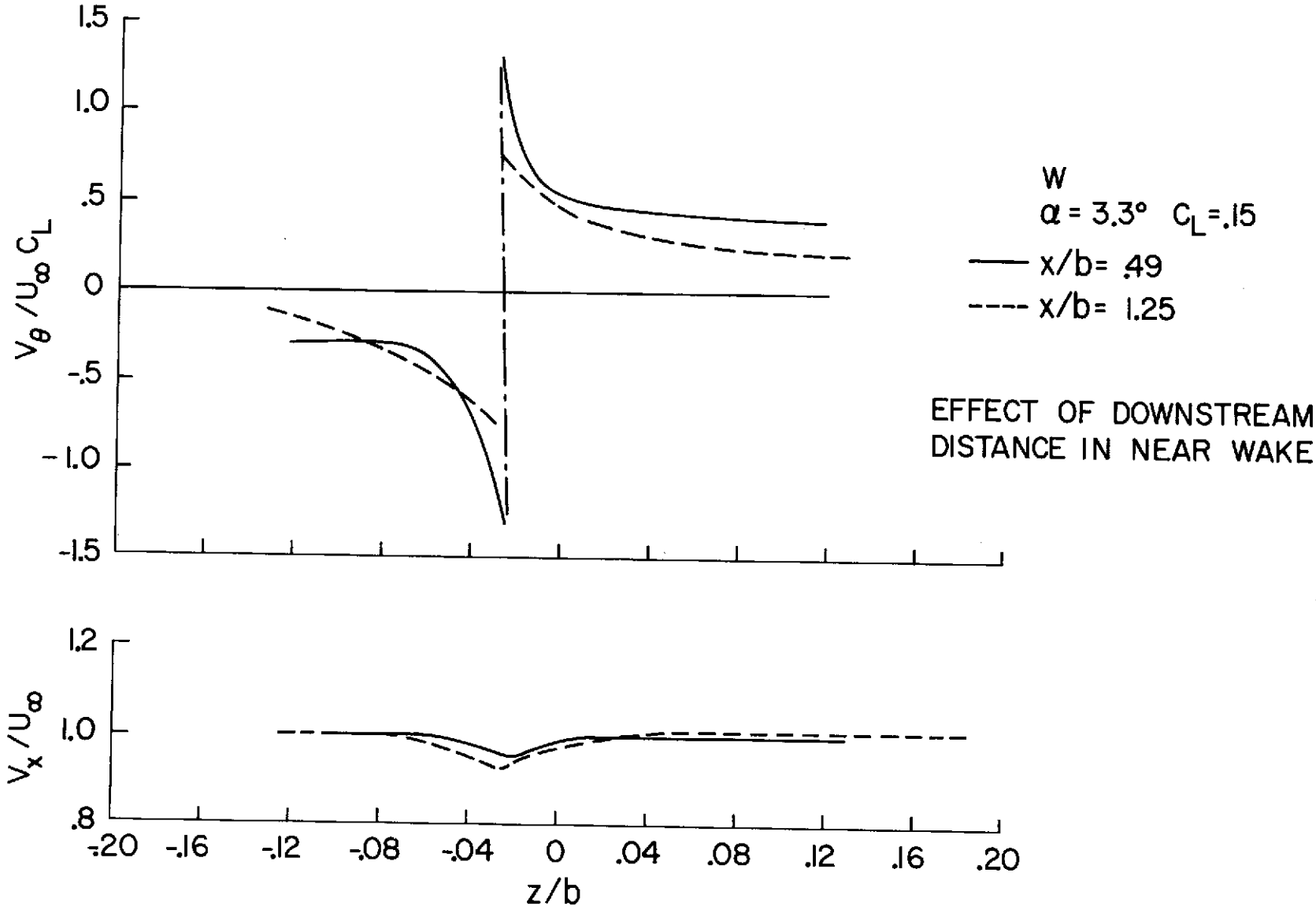
1.5
1.0
.5
0
-.5
-1.0
-1.5
$V_\theta / U_\infty C_L$
W
$\alpha = 3.3°$ $C_L = .15$
x/b= .49
x/b= 1.25
EFFECT OF DOWNSTREAM DISTANCE IN NEAR WAKE
1.2
1.0
.8
V_x / U_∞
-.20
-.16
-.12
-.08
-.04
0
.04
.08
.12
.16
.20
z/b

Figure 7

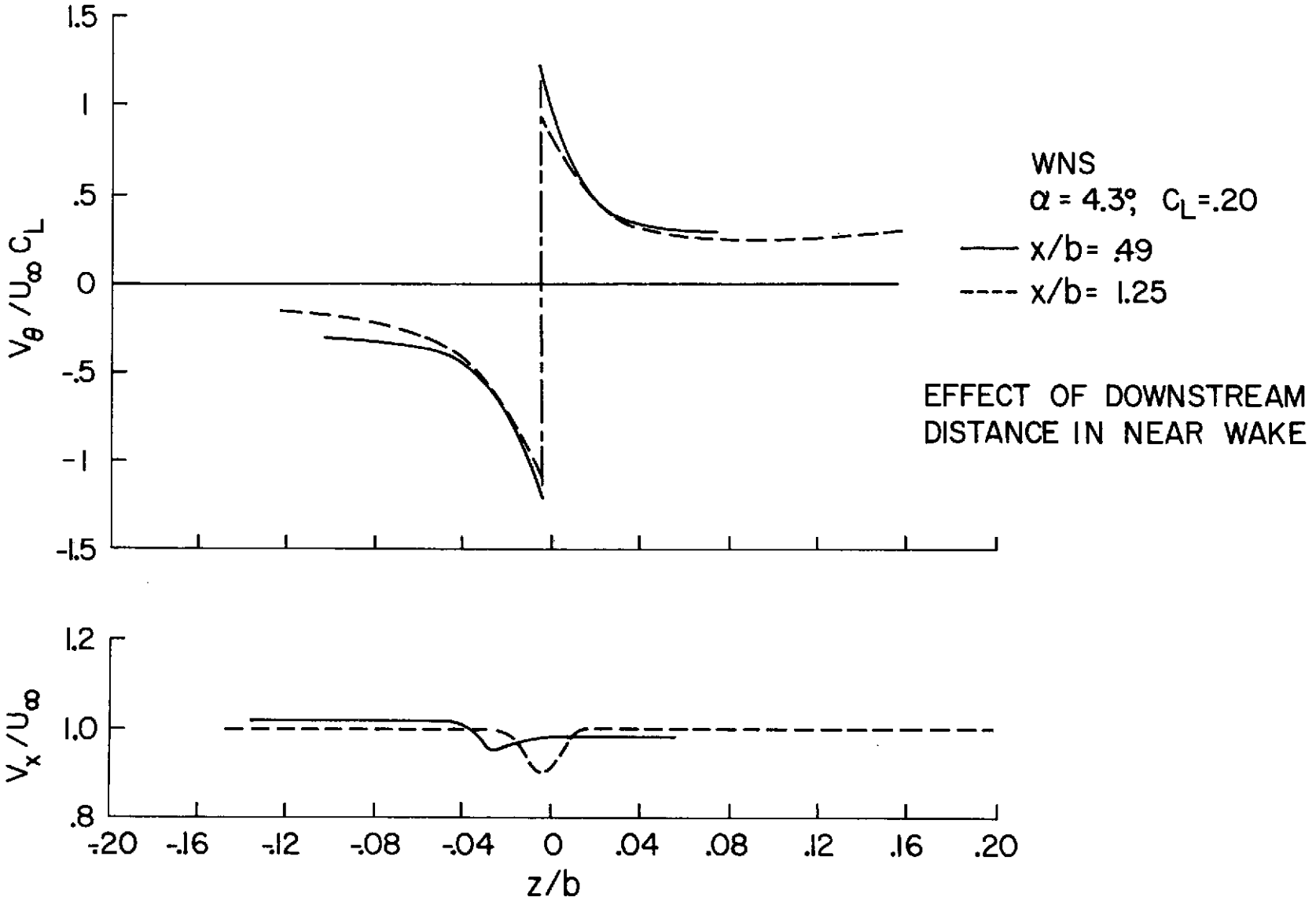
1.5
1
.5
0
-.5
-1
-1.5
$V_\theta / U_\infty C_L$
WNS
α = 4.3°; C_L=.20
x/b= .49
x/b= 1.25
EFFECT OF DOWNSTREAM
DISTANCE IN NEAR WAKE
1.2
1.0
.8
V_x / U_∞
-.20
-.16
-.12
-.08
-.04
0
.04
.08
.12
.16
.20
z/b

Figure 8

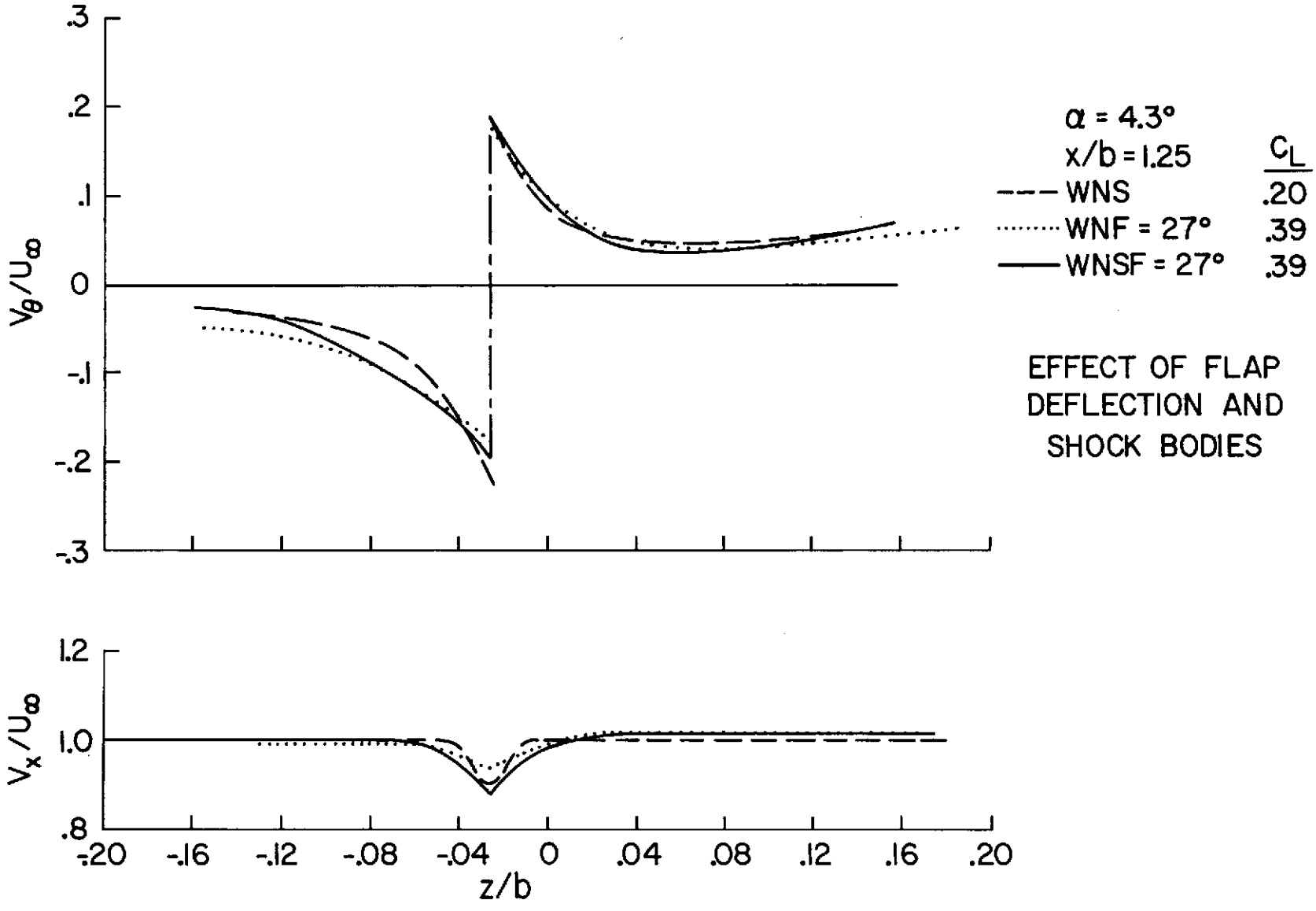
.3
.2
.1
0
-.1
-.2
-.3
V_θ/U_∞
1.2
1.0
.8
V_x/U_∞
-.20
-.16
-.12
-.08
-.04
0
.04
.08
.12
.16
.20
z/b
α = 4.3°
x/b = 1.25
C_L
--- WNS .20
····· WNF = 27° .39
—— WNSF = 27° .39
EFFECT OF FLAP DEFLECTION AND SHOCK BODIES

Figure 9

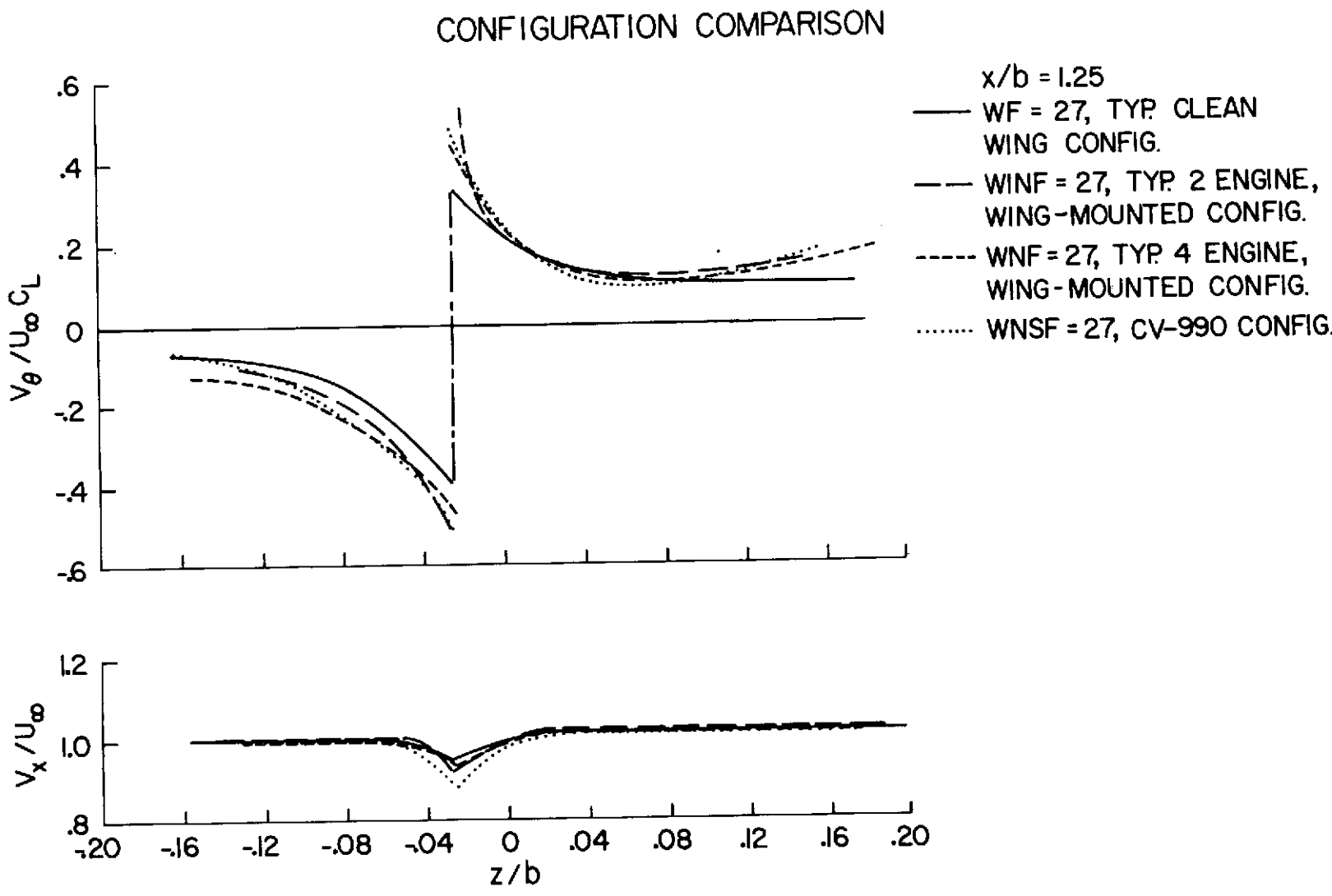
CONFIGURATION COMPARISON
x/b = 1.25
WF = 27, TYP. CLEAN WING CONFIG.
WINF = 27, TYP. 2 ENGINE, WING-MOUNTED CONFIG.
WNF = 27, TYP. 4 ENGINE, WING-MOUNTED CONFIG.
WNSF = 27, CV-990 CONFIG.
$V_\theta / U_\infty C_L$
.6
.4
.2
0
-.2
-.4
-.6
V_x / U_∞
1.2
1.0
.8
-.20
-.16
-.12
-.08
-.04
0
.04
.08
.12
.16
.20
z/b

Figure 10

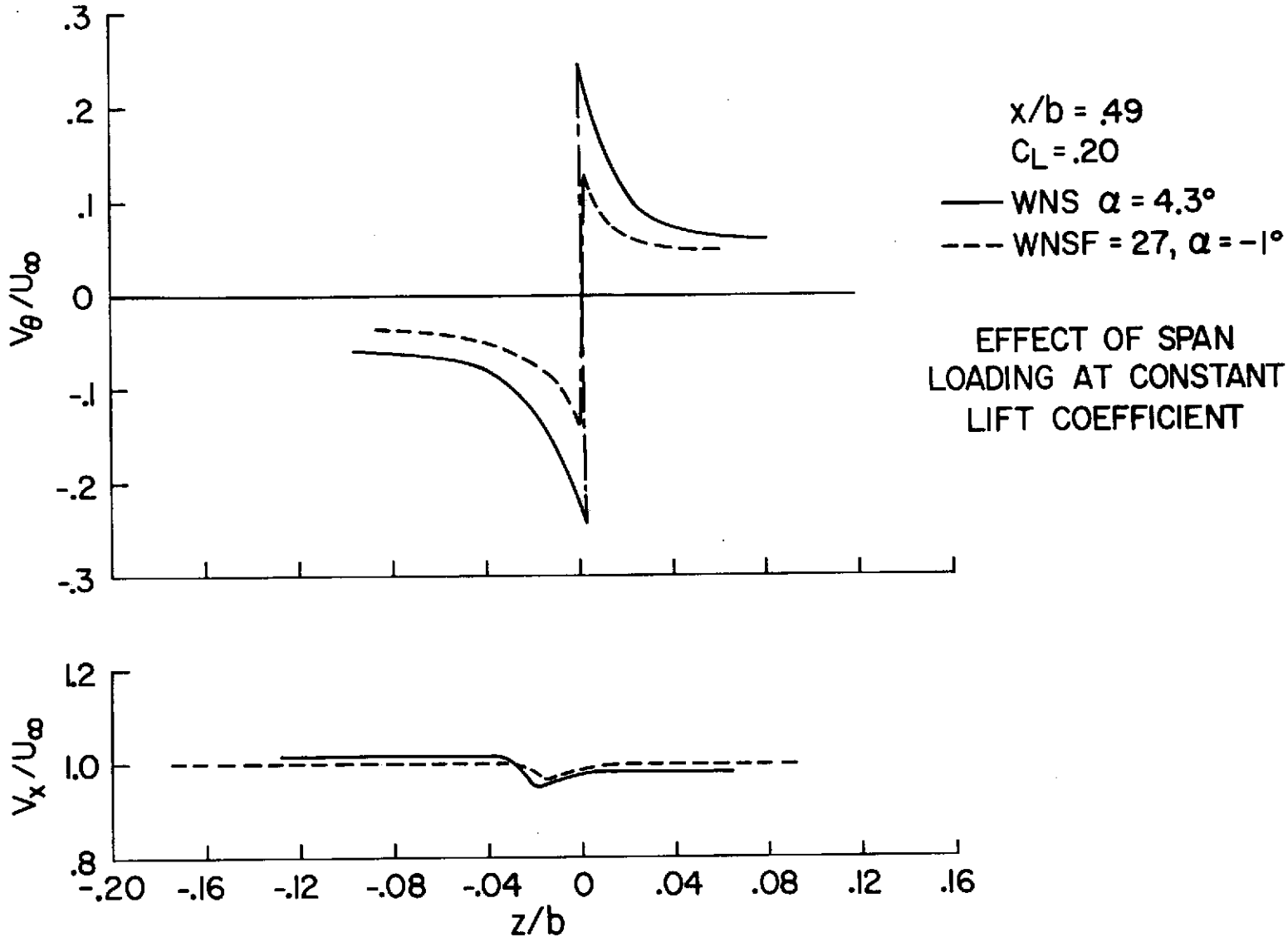
.3
.2
.1
0
-.1
-.2
-.3
V_θ/U_∞
x/b = .49
C_L = .20
WNS α = 4.3°
WNSF = 27, α = -1°
EFFECT OF SPAN LOADING AT CONSTANT LIFT COEFFICIENT
1.2
1.0
.8
V_x/U_∞
-.20
-.16
-.12
-.08
-.04
0
.04
.08
.12
.16
z/b

Figure 11

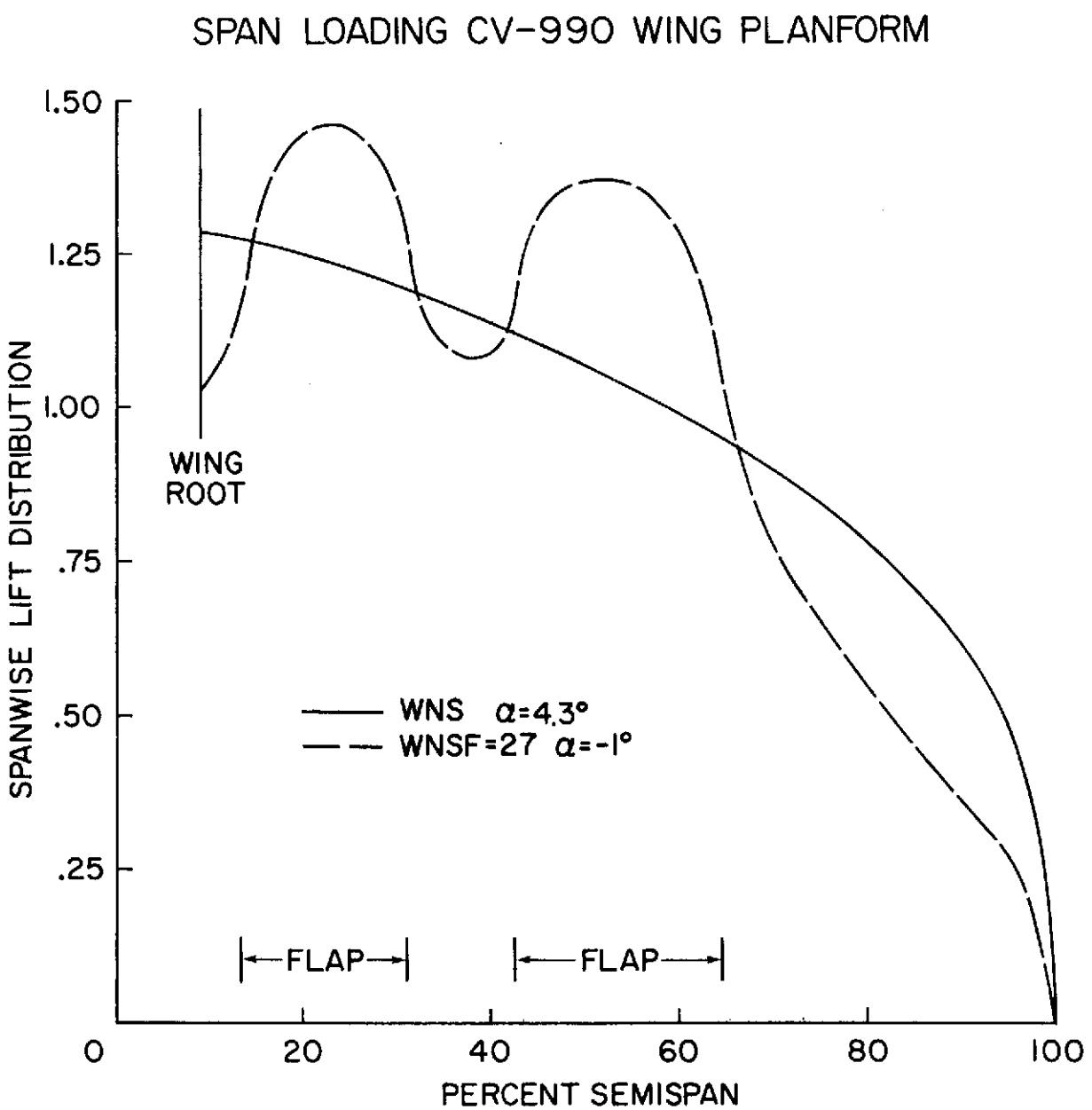
SPAN LOADING CV-990 WING PLANFORM
SPANWISE LIFT DISTRIBUTION
1.50
1.25
1.00
.75
.50
.25
WING ROOT
WNS α=4.3°
WNSF=27 α=-1°
FLAP
FLAP
0
20
40
60
80
100
PERCENT SEMISPAN

Figure 12

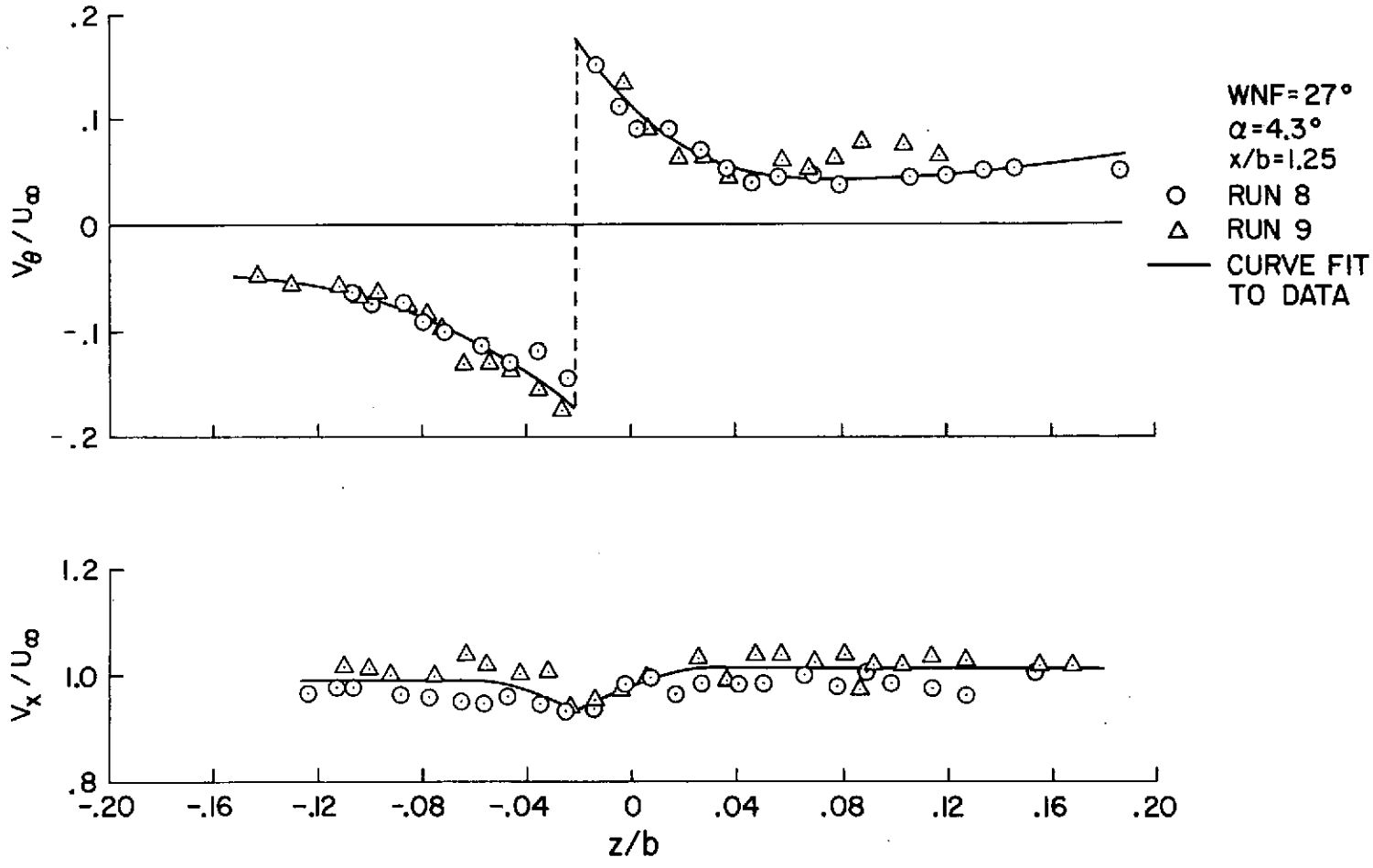
.2
.1
0
-.1
-.2
V_θ / U_∞
1.2
1.0
.8
V_x / U_∞
-.20
-.16
-.12
-.08
-.04
0
.04
.08
.12
.16
.20
z/b
WNF=27°
α=4.3°
x/b=1.25
RUN 8
RUN 9
CURVE FIT TO DATA

Figure A1

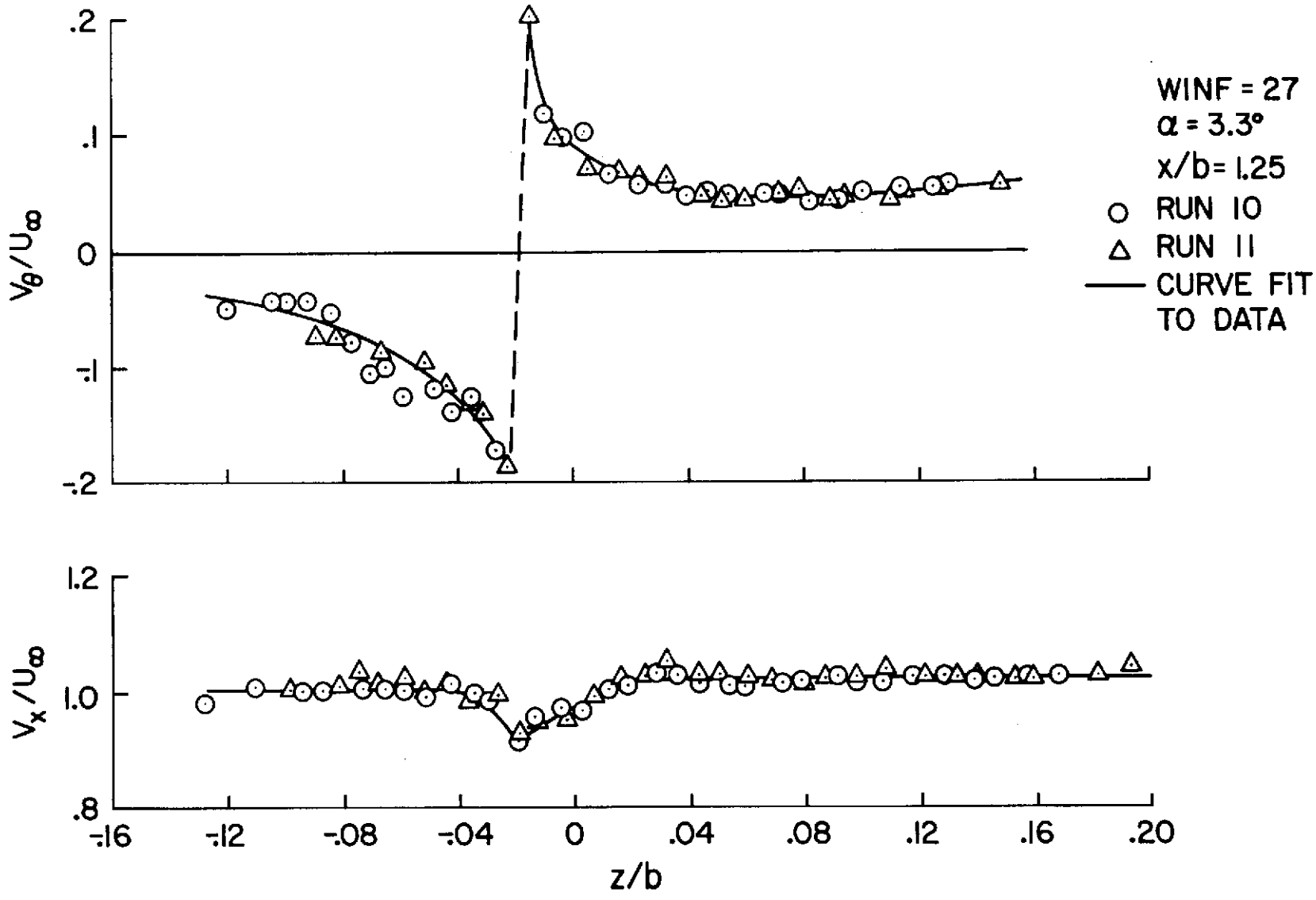
.2
.1
0
-.1
-.2
V_θ/U_∞
1.2
1.0
.8
V_x/U_∞
-.16
-.12
-.08
-.04
0
.04
.08
.12
.16
.20
z/b
WINF = 27
α = 3.3°
x/b= 1.25
RUN 10
RUN 11
CURVE FIT TO DATA

Figure A2

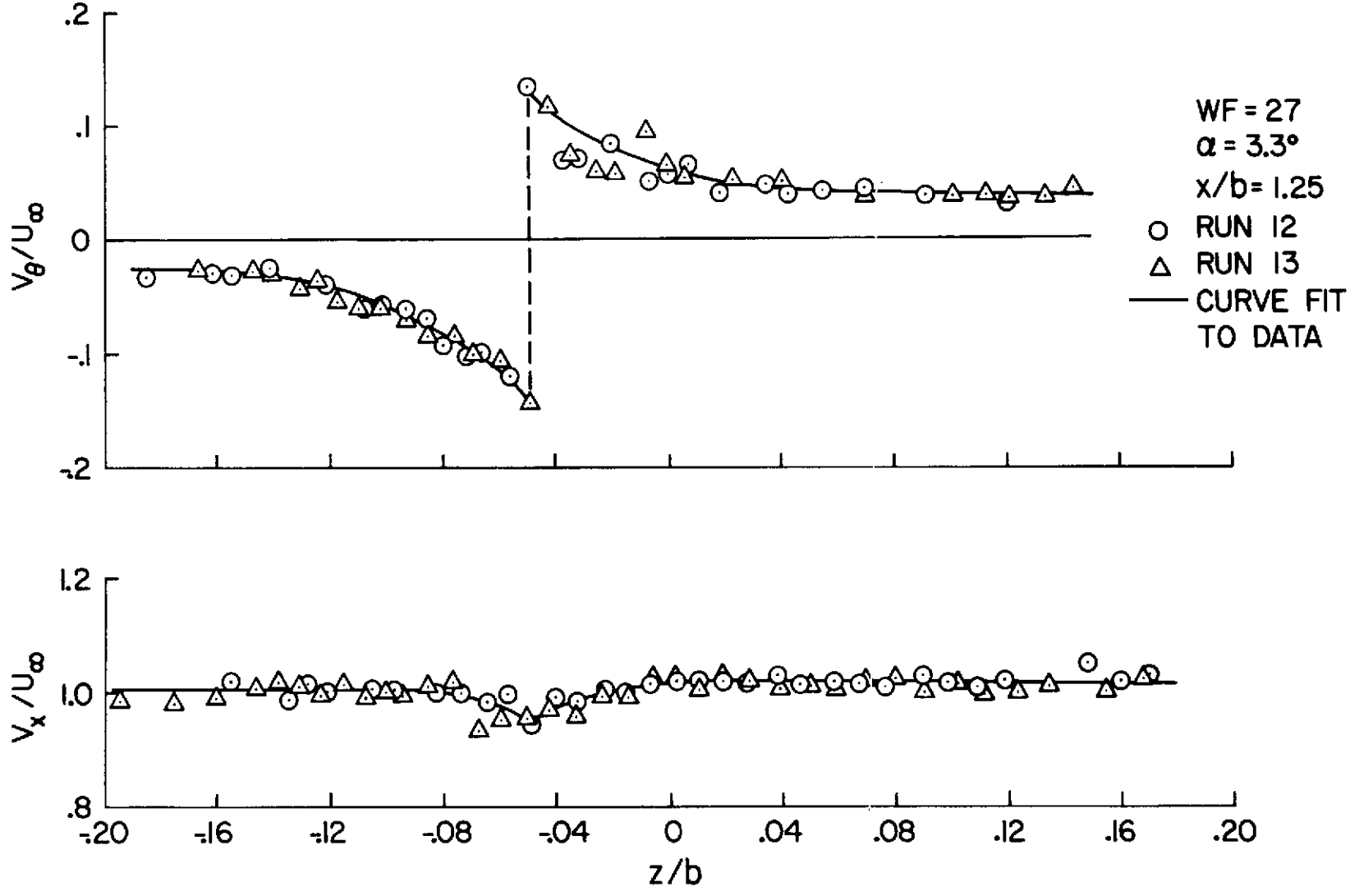
.2
.1
0
-.1
-.2
V_θ/U_∞
WF = 27
α = 3.3°
x/b = 1.25
RUN 12
RUN 13
CURVE FIT TO DATA
1.2
1.0
.8
V_x/U_∞
-.20
-.16
-.12
-.08
-.04
0
.04
.08
.12
.16
.20
z/b

Figure A3

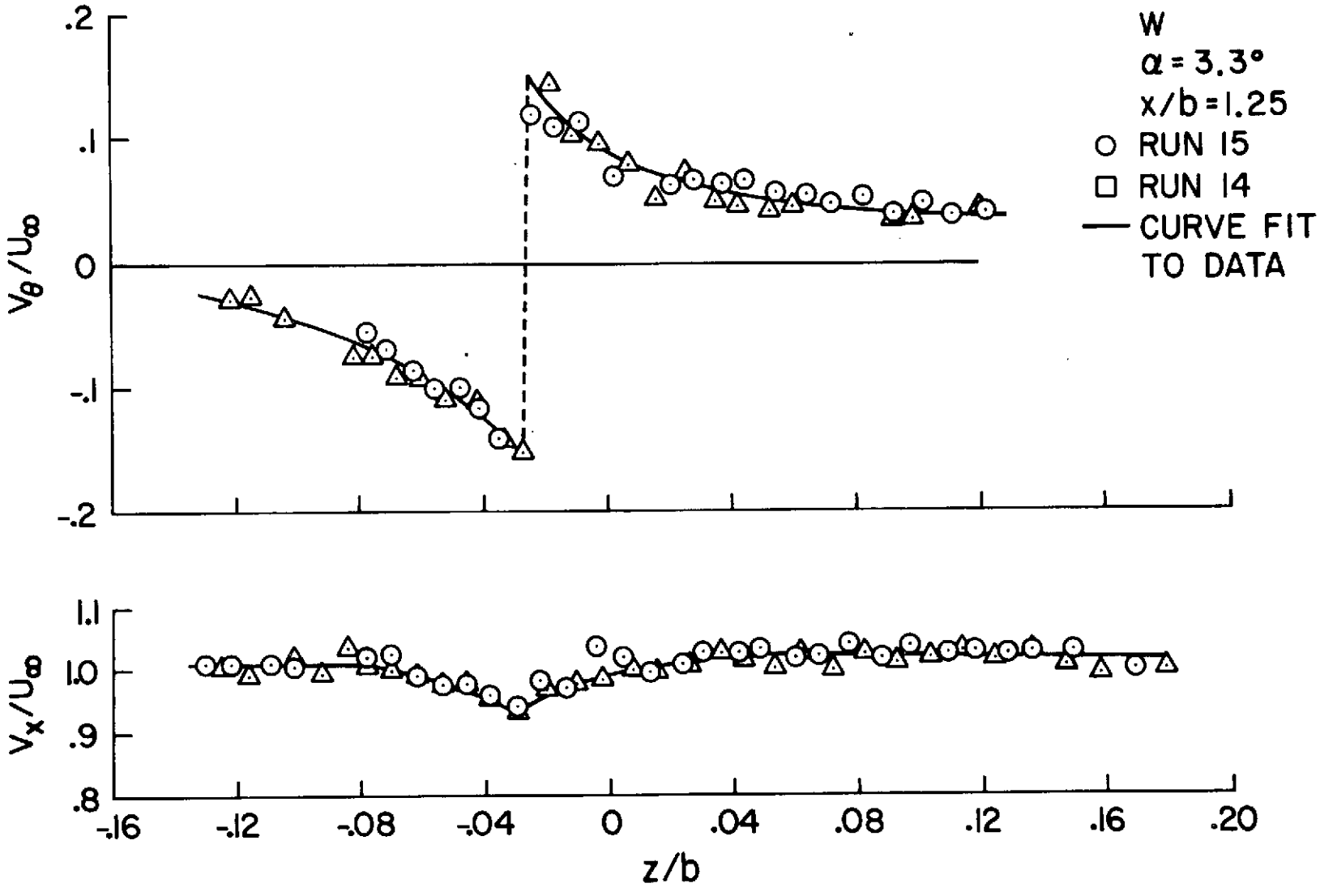
W
α = 3.3°
x/b = 1.25
RUN 15
RUN 14
CURVE FIT TO DATA
V_θ/U_∞
V_x/U_∞
z/b
.2
.1
0
-.1
-.2
1.1
1.0
.9
.8
-.16
-.12
-.08
-.04
0
.04
.08
.12
.16
.20

Figure A4

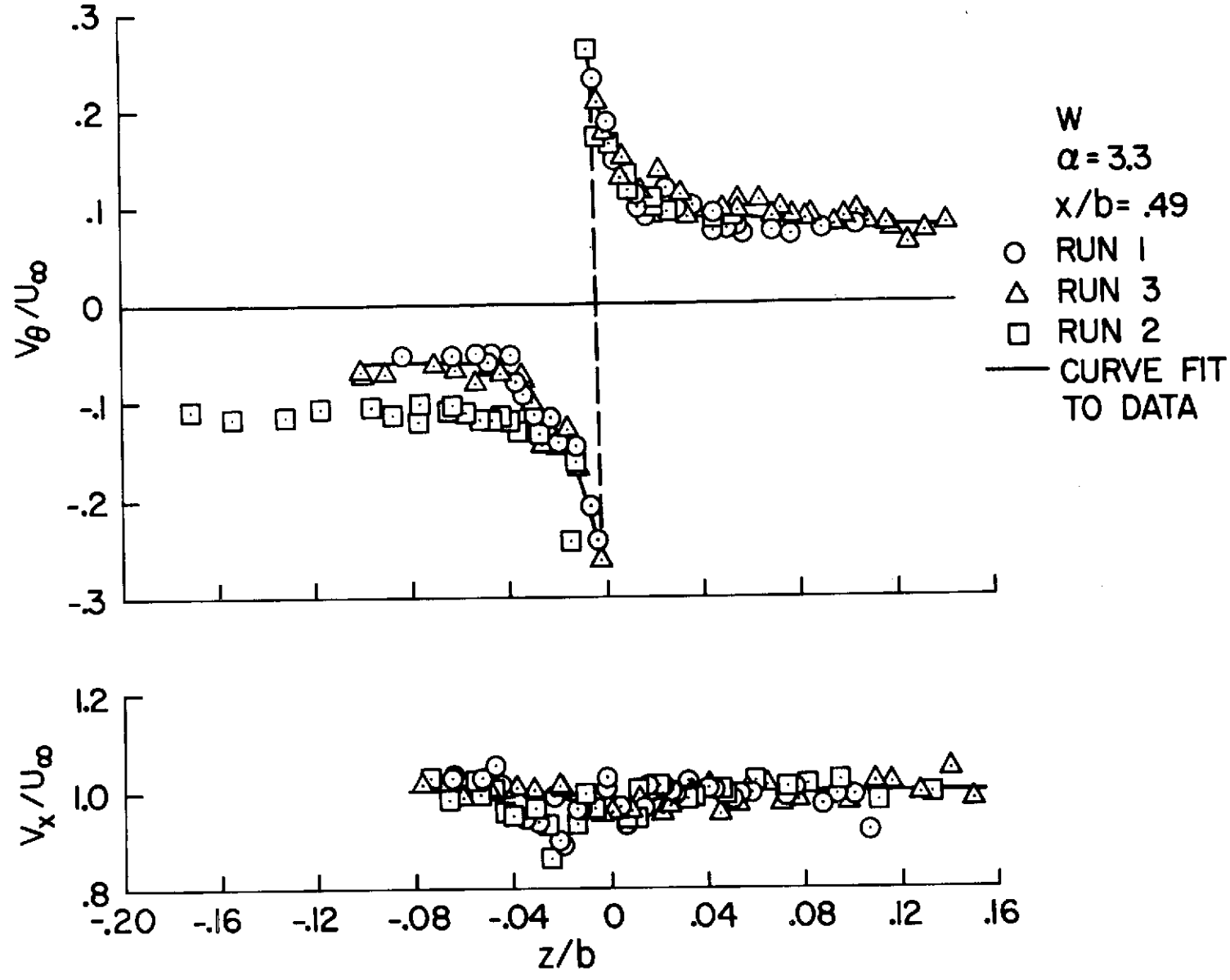
.3
.2
.1
0
-.1
-.2
-.3
V_θ/U_∞
W
α = 3.3
x/b= .49
RUN 1
RUN 3
RUN 2
CURVE FIT TO DATA
1.2
1.0
.8
V_x/U_∞
-.20
-.16
-.12
-.08
-.04
0
.04
.08
.12
.16
z/b

Figure A5

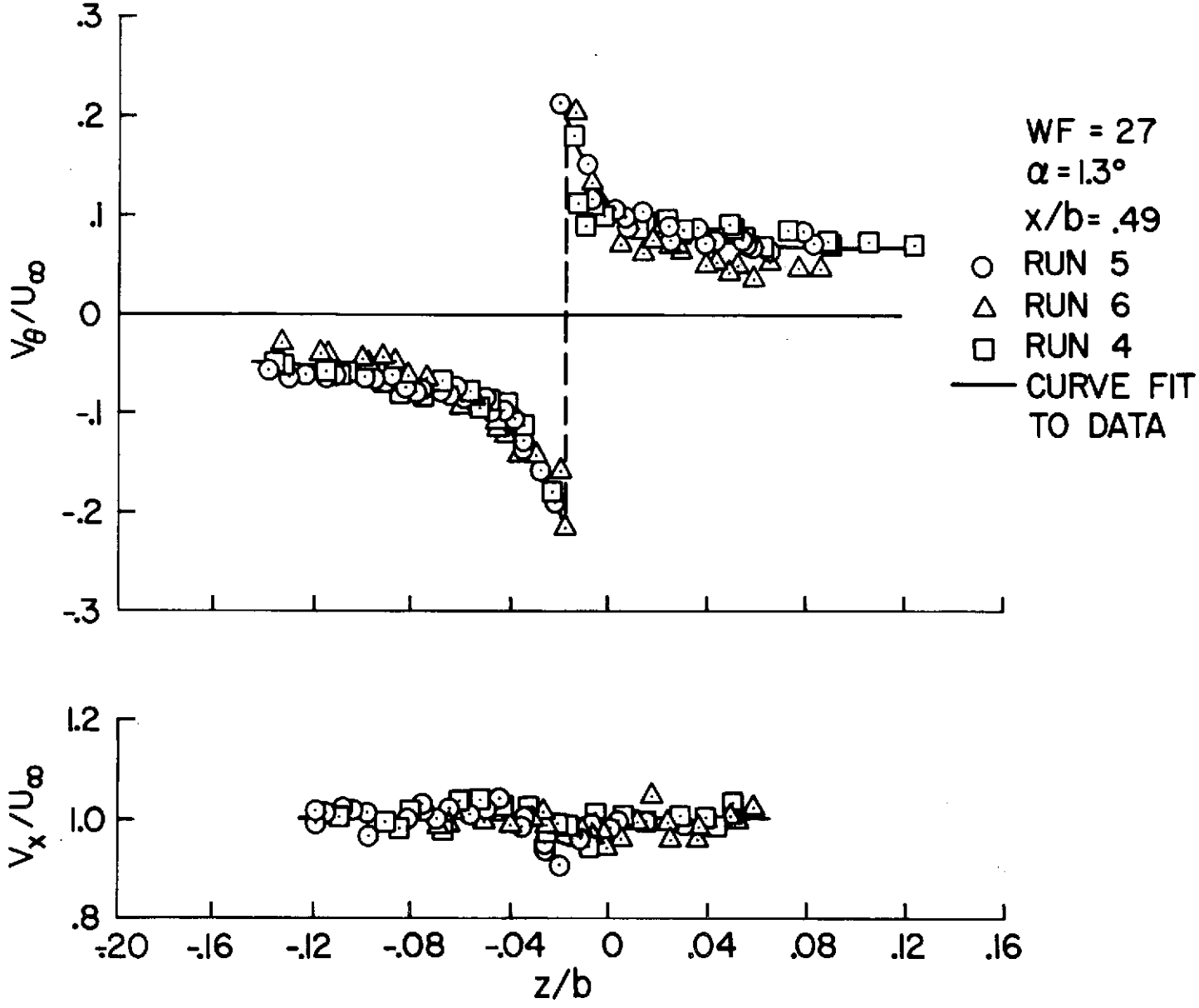
.3
.2
.1
0
-.1
-.2
-.3
V_θ/U_∞
WF = 27
α = 1.3°
x/b = .49
RUN 5
RUN 6
RUN 4
CURVE FIT TO DATA
1.2
1.0
.8
V_x/U_∞
-.20
-.16
-.12
-.08
-.04
0
.04
.08
.12
.16
z/b

Figure A6

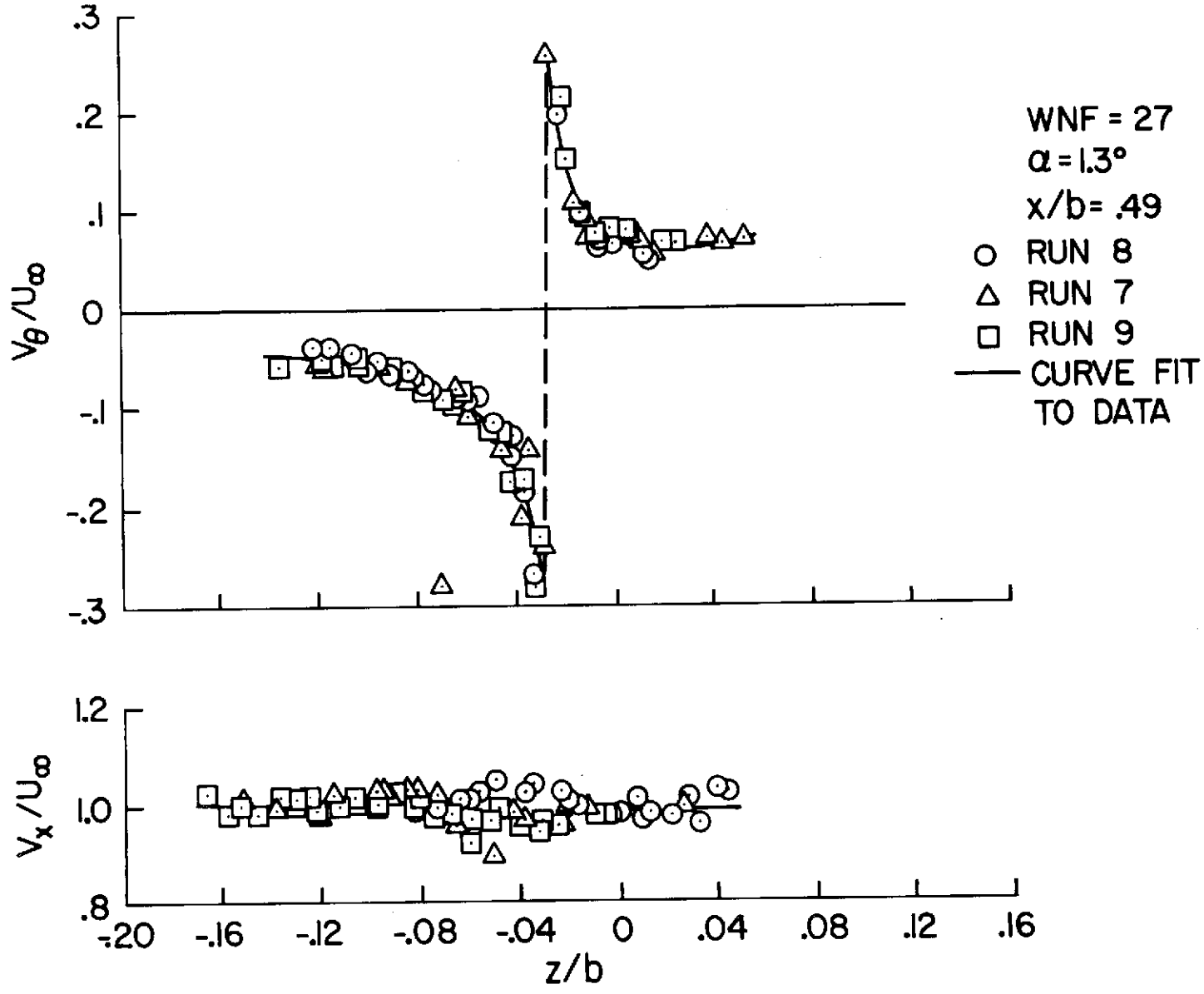
.3
.2
.1
0
-.1
-.2
-.3
V_θ/U_∞
WNF = 27
α = 1.3°
x/b = .49
RUN 8
RUN 7
RUN 9
CURVE FIT TO DATA
1.2
1.0
.8
V_x/U_∞
-.20
-.16
-.12
-.08
-.04
0
.04
.08
.12
.16
z/b

Figure A7

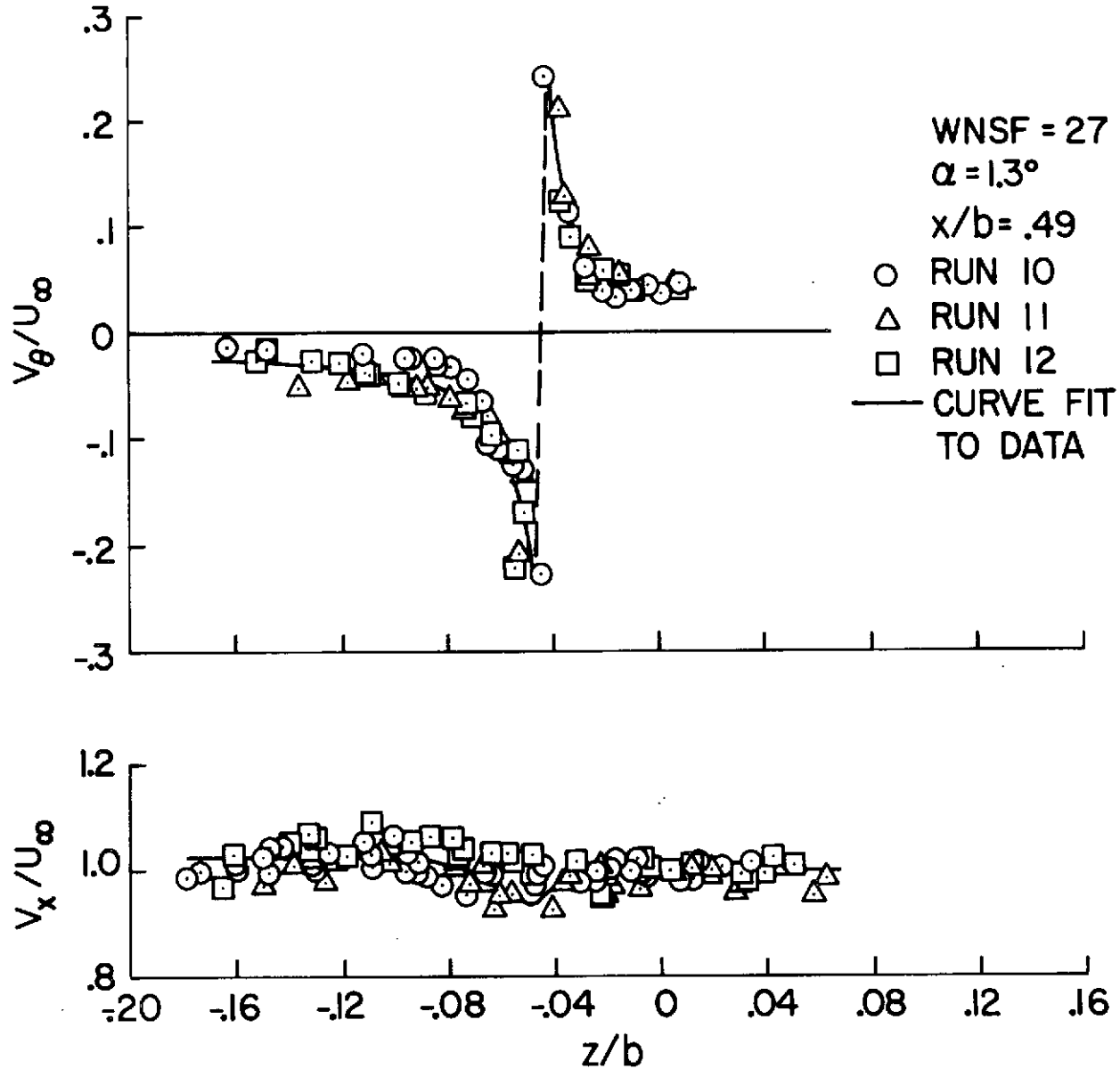
.3
.2
.1
0
-.1
-.2
-.3
V_θ/U_∞
WNSF = 27
α = 1.3°
x/b = .49
RUN 10
RUN 11
RUN 12
CURVE FIT TO DATA
1.2
1.0
.8
V_x/U_∞
-.20
-.16
-.12
-.08
-.04
0
.04
.08
.12
.16
z/b

Figure A8

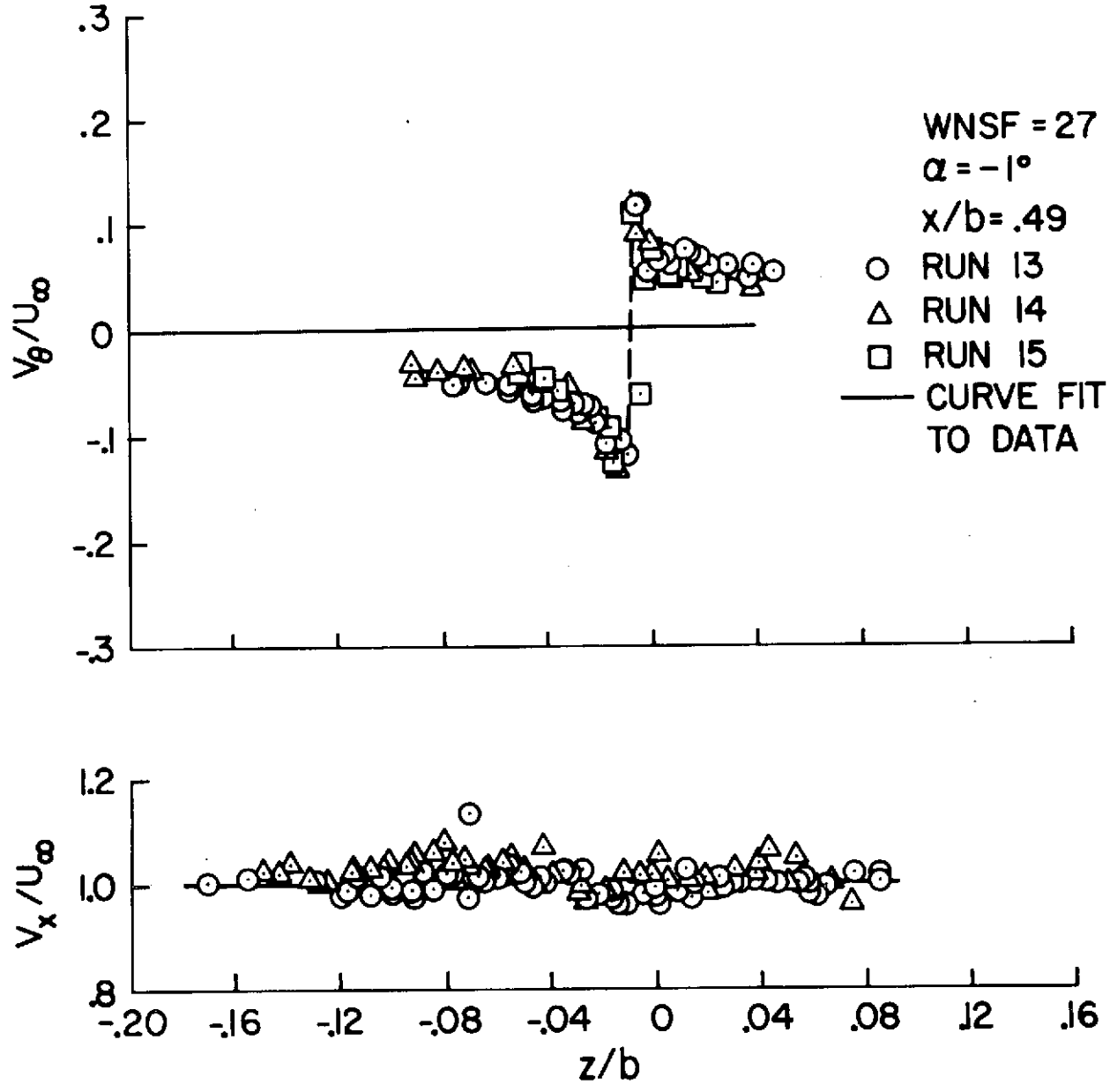
.3
.2
.1
0
-.1
-.2
-.3
V_θ/U_∞
WNSF = 27
α = −1°
x/b = .49
RUN 13
RUN 14
RUN 15
CURVE FIT TO DATA
1.2
1.0
.8
V_x/U_∞
-.20
-.16
-.12
-.08
-.04
0
.04
.08
.12
.16
z/b

Figure A9

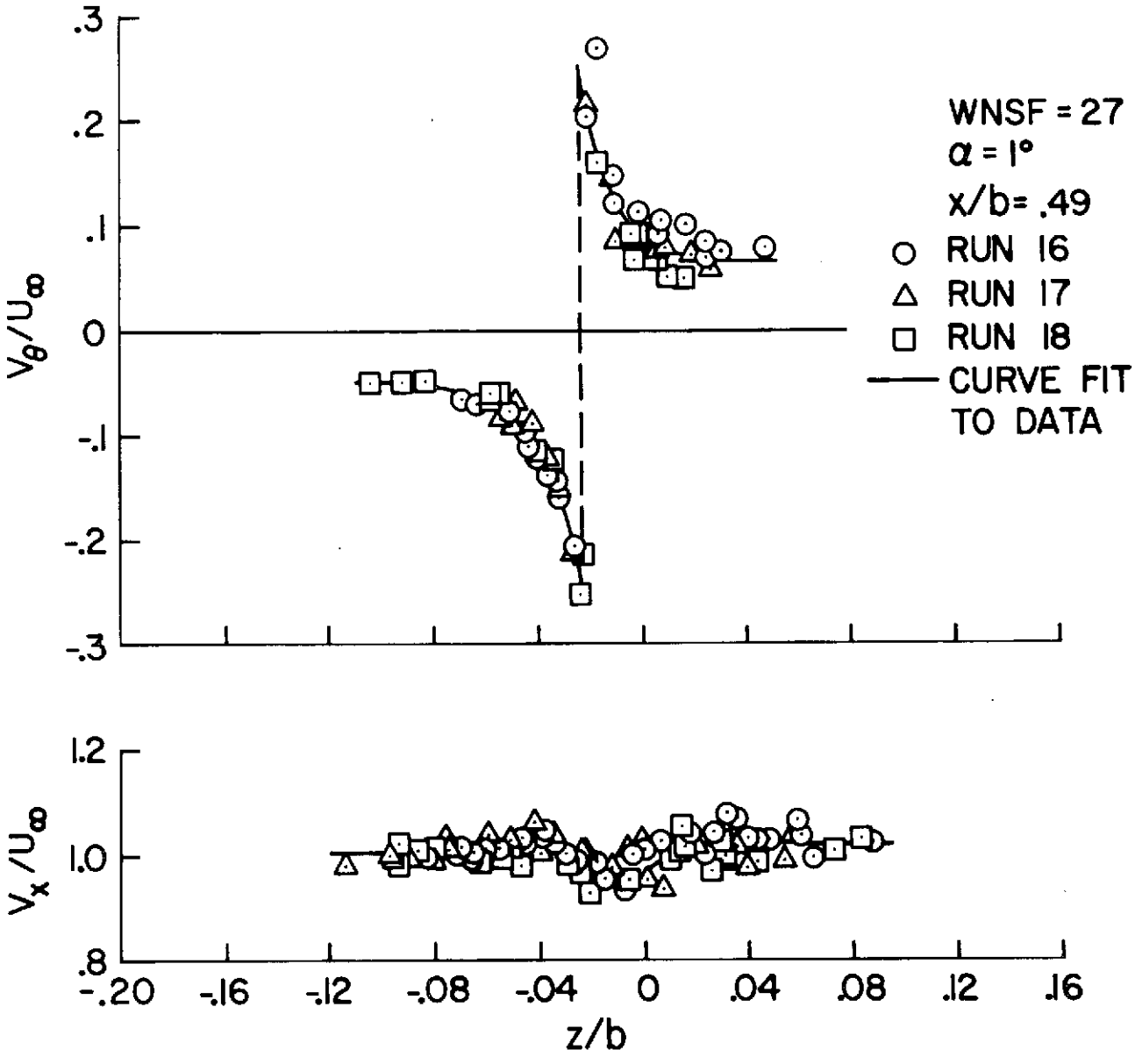
.3
.2
.1
0
-.1
-.2
-.3
V_θ/U_∞
WNSF = 27
α = 1°
x/b= .49
RUN 16
RUN 17
RUN 18
CURVE FIT TO DATA
1.2
1.0
.8
V_x/U_∞
-.20
-.16
-.12
-.08
-.04
0
.04
.08
.12
.16
z/b

Figure A10

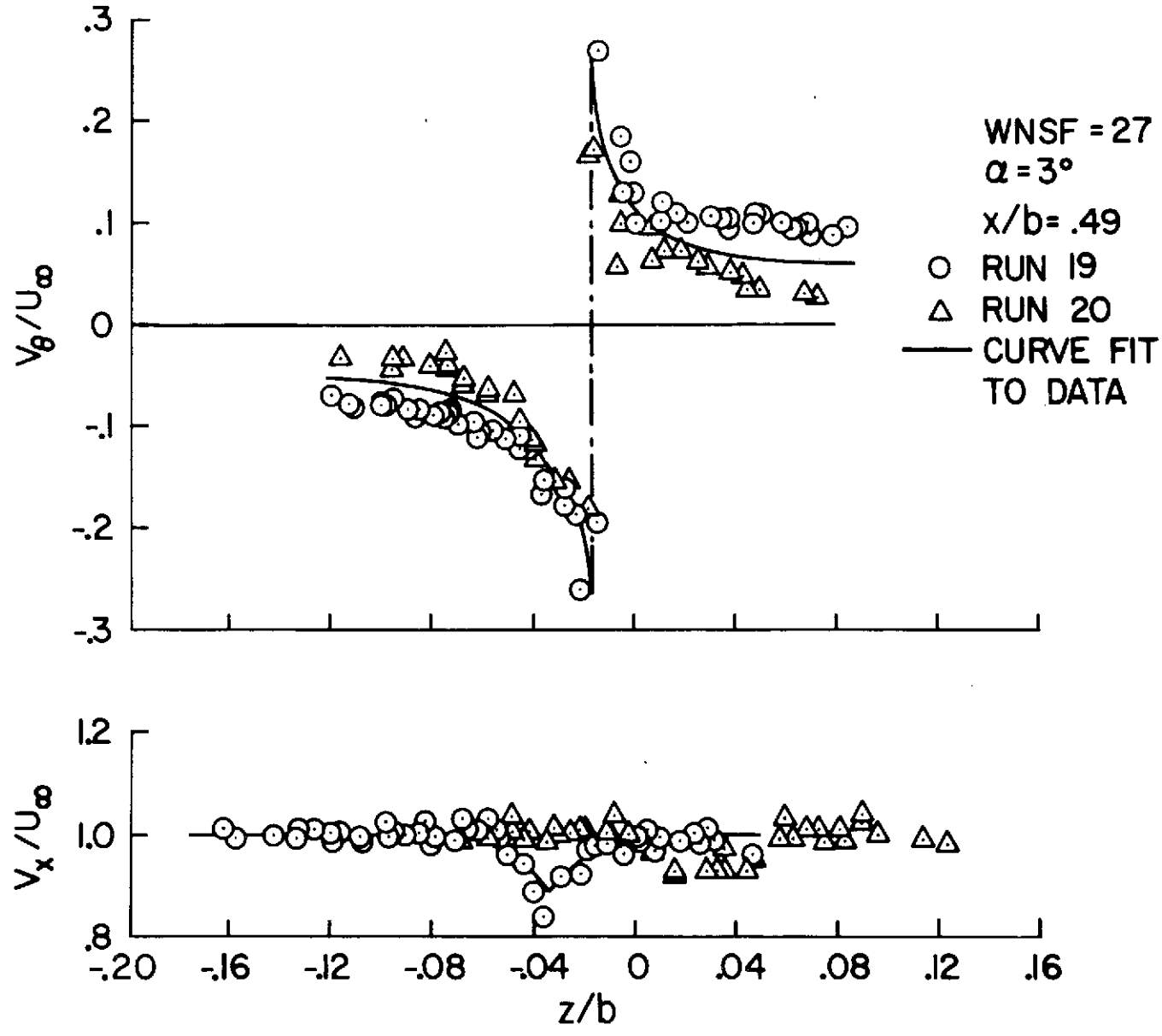
.3
.2
.1
0
-.1
-.2
-.3
V_θ/U_∞
WNSF = 27
α = 3°
x/b = .49
RUN 19
RUN 20
CURVE FIT TO DATA
1.2
1.0
.8
V_x/U_∞
-.20
-.16
-.12
-.08
-.04
0
.04
.08
.12
.16
z/b

Figure A11

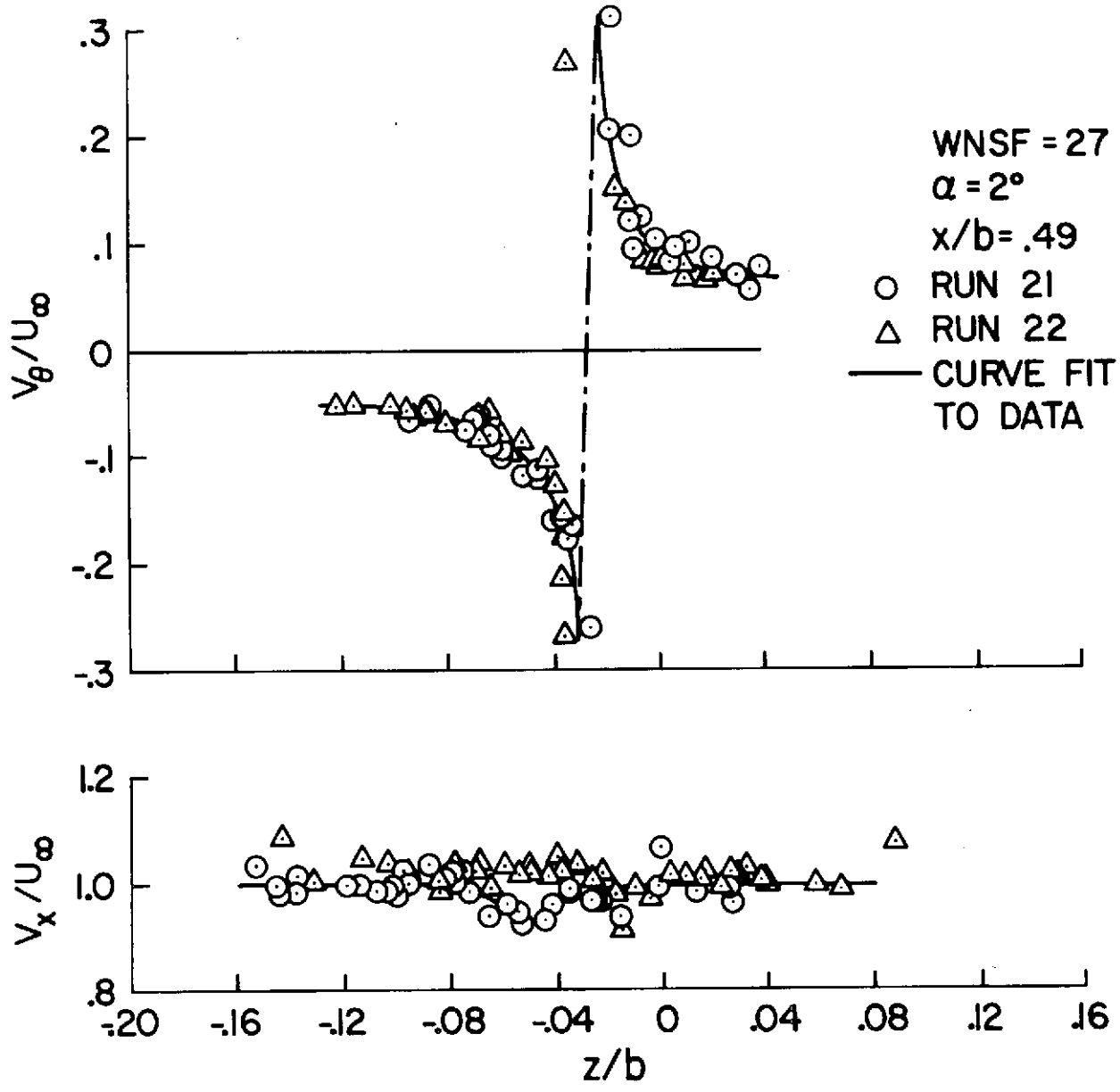
.3
.2
.1
0
-.1
-.2
-.3
V_θ/U_∞
WNSF = 27
α = 2°
x/b = .49
RUN 21
RUN 22
CURVE FIT TO DATA
1.2
1.0
.8
V_x/U_∞
-.20
-.16
-.12
-.08
-.04
0
.04
.08
.12
.16
z/b

Figure A12

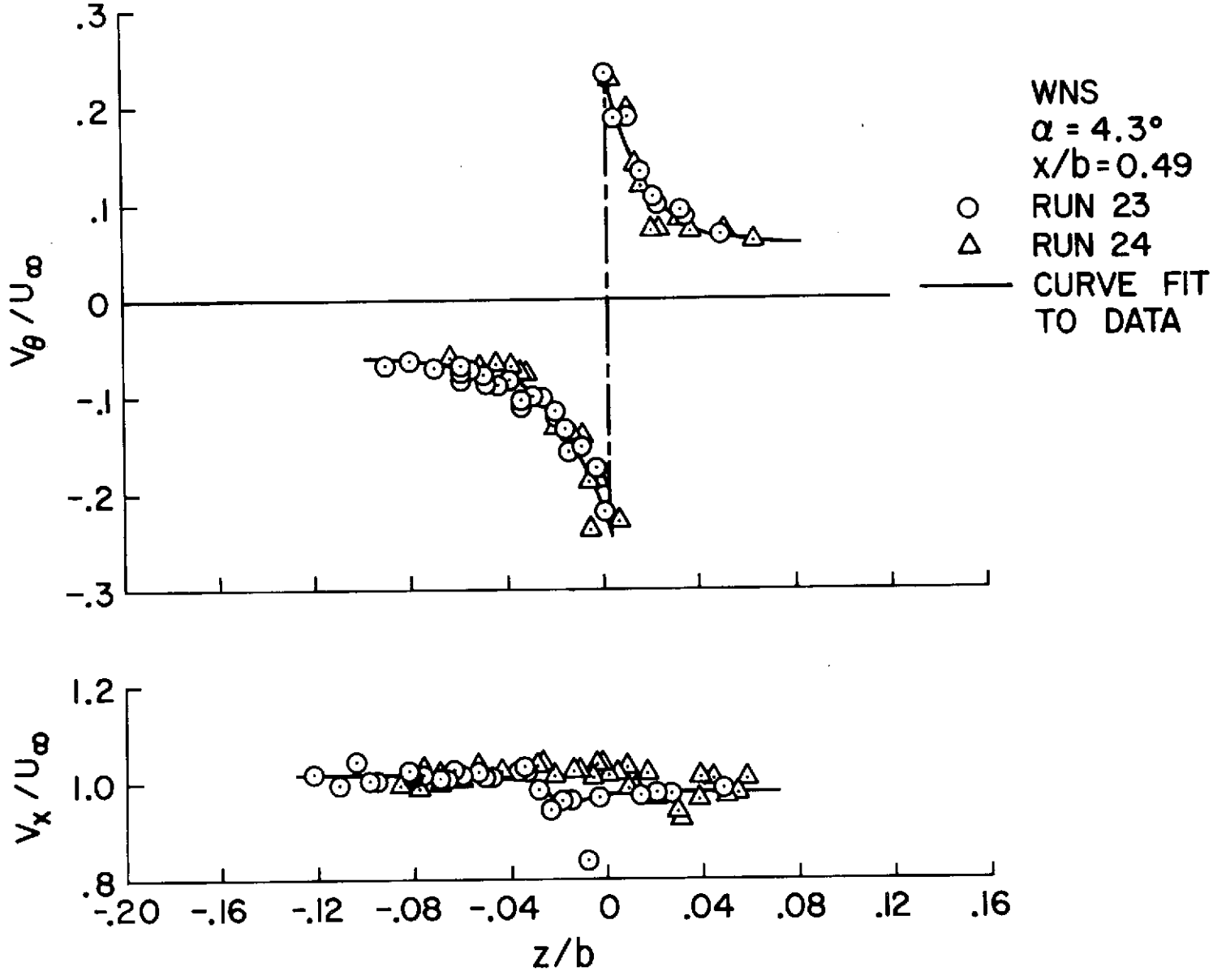
.3
.2
.1
0
-.1
-.2
-.3
V_θ / U_∞
WNS
$\alpha = 4.3°$
x/b=0.49
RUN 23
RUN 24
CURVE FIT TO DATA
1.2
1.0
.8
V_x / U_∞
-.20
-.16
-.12
-.08
-.04
0
.04
.08
.12
.16
z/b

Figure A13